Trapped Heterogeneous Waters in Eddies Cores from In Situ Data

Yan Barabinot[1], **Sabrina Speich**[1], **Xavier Carton**[2]

[1]Ecole Normale Supérieure, Laboratoire de Météorologie Dynamique (LMD), 24 rue Lhomond, Paris 75005, France
[2]Université de Bretagne Occidentale (UBO), Laboratoire d'Océanographie Physique et Spatiale (LOPS), IUEM, rue Dumont Durville, Plouzané 29280, France

Key Points:

- Some eddies are not classified as materially coherent using only surface data, but they are when their three-dimensional structure is studied.
- The outermost closed contour of the Brunt-Vaisala frequency is a good approximation of the boundary of the materially coherent eddy core.
- The vertical resolution of the velocity data and the horizontal resolution of the hydrological data lead to uncertainties in the calculation of their gradients

Corresponding author: Yan Barabinot, `yan.barabinot@ens-paris-saclay.fr`

Abstract

In this paper we analyze the effect of material coherence on the transport properties of 9 eddies sampled during research cruises. We check the accuracy of our data and, after reviewing different definitions of coherence, we assess whether these eddies have retained a heterogeneous water mass in their cores. T, S anomalies on isopycnal surfaces are computed to highlight the different thermohaline properties between the eddy core and its surroundings. The maximum of the tracer anomaly is often located below the pycnocline. We find that while some of these eddies are not coherent according to surface data only, they are when their entire 3D structure is considered. We then present two methods for extrapolating eddy volumes from a single hydrographic section. The volume obtained from T,S anomalies on isopycnical surfaces is compared with that obtained by other criteria. Our results show that the outermost closed contour of the Brunt-Väisäla frequency is a good approximation for the eddy boundary when calculating its volume.

Plain Language Summary

Mesoscale eddies are ubiquitous rotating currents in the ocean. They are considered one of the most important sources of ocean variability because they can live for months and transport and mix heat, salt, and other properties within and between ocean basins. They have been studied extensively from satellite observations, mainly altimetry, because they are often at or near the ocean surface. However, observations of their 3D structure are rare, and calculations of eddy transport are often approximated without precise knowledge of their true vertical extent. Here, we analyze the full 3D structures of mesoscale eddies sampled during 9 oceanographic cruises to assess their ability to trap a water mass that is different from the surrounding water mass. Such eddies are called "materially coherent" and contribute to the total heat and salt transport across basins. In this study, however, we found that coherence properties vary with depth. For example, mesoscale eddies can be found to be nonmaterially coherent if we consider only their surface properties, but materially coherent if we consider their characteristics at depth. As a result, future studies cannot rely solely on satellite data to evaluate heat and salt transport.

1 Introduction

Mesoscale eddies are ubiquitous energetic structures in the ocean and are one of the major sources of ocean variability (Stammer, 1997; Wunsch, 1999). They are thought to have a major influence on the propagation of hydrological properties by advecting them over long distances and timescales (McWilliams, 1985). The lifetime of such structures often exceeds several months and can reach several years (Laxenaire et al., 2018; Ioannou et al., 2022), highlighting their resilience and their "coherence".

The word "coherence" was first introduced to describe specific structures in turbulent boundary layers. This terminology was used to imply that the near-wall region contains certain basic flow modules or structures that give rise to the apparently ordered development observed in the wall layer (Kline et al., 1967; Crow & Champagne, 1971; Roshko, 1976). Thus, "coherence" was first a concept of persistence in time and of "order/disorder". Then these structures were studied more and more, and other definitions, involving vorticity, appeared. (A. Hussain & Zaman, 1980; A. F. Hussain, 1986; Zaman & Hussain, 1981) proposed that a "coherent" structure was characterized by an instantaneous component of large-scale vorticity that dominated the rest of the flow. "Coherence was thus a concept defined in space and time, but remained qualitative. Later, Charney (1971); Herring (1980); Hua and Haidvogel (1986); McWilliams (1984, 1989) applied the concept of "coherence" to geophysical fluid dynamics, especially for mesoscale eddies, and implicitly proposed that a "coherent eddy" was a temporally persistent vortex of large radius.

With the advent of altimetry, oceanic eddies were often characterized by sea surface height anomalies organized as a set of concentric closed isolines. These isolines could be followed in time via a (mostly) continuous trajectory of their center (Chaigneau et al., 2009; Chelton et al., 2011; Pegliasco et al., 2016; Zhang et al., 2016). As these studies investigated the persistence of the vortex flow in time, they were related to the concept of coherence defined by McWilliams (1984, 1989). In our article we will call this vision of coherence *Kinematic Coherence* (KC). However, KC is only qualitative: indeed, different studies have provided different definitions of the eddy boundary using satellite altimetry data.

For a quantitative characterization of eddy coherence, oceanographers initially relied on flow stability criteria (e.g. Fjörtoft, 1950; Eliassen, 1951; Pedlosky, 1964; Bretherton, 1966; Hoskins, 1974; Carton & McWilliams, 1989; Ripa, 1991). However, recent studies have shown that even in the presence of moderate, localized instability, a vortex can remain kinematically coherent for long periods of time (de Marez et al., 2020). Conversely, long-lived vortices can become unstable, stretch, shed filaments, and disappear under the influence of ambient velocity shear (Carton, 2001; Carton et al., 2010). Therefore, vortex stability is not equivalent to *kinematic coherence*.

Nor is KC equivalent to exact eddy invariance: indeed, an eddy can shed filaments or incorporate water masses into its core by lateral diffusion or entrainment. These processes occur at the eddy boundary, where the strain is intense. Conversely, eddy cores are loci of stronger vorticity than strain. Consequently, Eulerian criteria for KC and for the determination of eddy shapes have been derived using these two quantities (Hunt et al., 1988; Ōkubo, 1970; Weiss, 1991; Chong et al., 1990; Tabor & Klapper, 1994).

In situ measurements have shown that mesoscale eddy cores contain different water masses from those of the surrounding environment. The core water masses are characteristic of the eddy formation region. Mesoscale eddies can transport these water masses over long distances (several thousand kilometers; see (Chelton et al., 2011; Dong & McWilliams, 2007; Zhang et al., 2014). To explain the robustness along the trajectory, Lagrangian approaches have been used to find coherence criteria. Flierl (1981) showed that when the rotational velocity of the vortex is higher than its translational velocity, fluid particles are trapped in the vortex core.

A new theory was then proposed by Haller (2000, 2005); Haller et al. (2015). First, Haller (2005) imposed a vortex coherence criterion to be invariant under a change of reference frame; he criticized the KC theory for being reference frame dependent and not objective. The Lagrangian Coherent Structures (LCS) framework was then proposed to construct an objective Lagrangian definition of a mesoscale vortex. In Haller's vision, a coherent vortex traps a mass of water in its core as it forms. This vortex ceases to be coherent when it loses its trapped water mass. We call this definition *Material Coherence* (MC). Objective Lagrangian criteria have been used by these authors to detect materially coherent vortices (Haller, 2015; Xia et al., 2022).

However, these criteria have mostly been applied using altimetry-derived geostrophic velocity fields; these 2D fields are not representative of the wide variety of oceanic eddies. In fact, eddy flow may be partially ageostrophic and not surface intensified. This is also true for eddies identified from satellite altimetry, as the observed sea surface dynamic height provides vertically integrated information about the local density field (e.g. Laxenaire et al., 2019, 2020). Furthermore, MC theory is based only on fluid flow and does not consider the potential permeability of the eddy boundary due to diffusion processes or lateral intrusion (Joyce, 1977, 1984; Ruddick et al., 2010). In particular, it ignores the fact that water masses can change their properties at the edge of eddies due to various types of instabilities. Finally, few long-lived MC eddies have been found compared to a larger number of KC eddies (Beron-Vera et al., 2013; Haller, 2015).

The MC definition of eddy coherence is rigorous: it describes how an eddy can trap and transport tracers over long distances. However, the MC view appears to be restrictive because it suggests that mesoscale eddies stop transporting water when the core loses its coherence, although an eddy can also advect a mass of water at its edge, creating a crown-like structure. Recent studies have shown a difference of more than 30% between the number of KC and MC eddies detected (Vortmeyer-Kley et al., 2019; Liu et al., 2019). This lack of consensus has implications for estimating tracer transport (Dong et al., 2014; Wang et al., 2015; Xia et al., 2022) and hence ocean mixing. The amount of tracer transported by mesoscale eddies appears to be larger using Eulerian criteria than Lagrangian criteria (see Figure 8 of (Beron-Vera et al., 2013)). The estimation of eddy mixing is highly dependent on the criterion used.

It should be noted that the KC and MC visions do not appear to be incompatible. In fact, altimetry and ARGO floats show that almost all KC eddies are associated with a thermohaline anomaly in their core. Thus, a kinematically coherent eddy can be a materially coherent eddy. In fact, homogeneous mesoscale eddies (eddies without a thermohaline anomaly in their core) are very rare in the ocean. A few are found in coastal regions, but they are very sensitive to bottom friction and interactions with topography and are therefore short-lived. The converse, MC implies KC, is also true, since the definition of MC requires an intense velocity field and kinematic coherence over a long period. While these two definitions are not exclusive, they are obviously not equivalent.

This brief review highlights several questions that studies should focus on: How can we apply these definitions of coherence to the 3D structure of eddies in the ocean? Is a single definition possible, taking into account the role of thermodynamics in the structure of oceanic eddies? Can we accurately estimate the contribution of eddies to global tracer transport? One approach to answer these questions is the concept of potential vorticity. It combines the two aspects of eddy coherence: the existence of closed trajectories within which it remains invariant (in the absence of forcing and mixing), and its strong association with the trapping of water masses (via isopycnal deviations). It is a materially conserved property of eddies. In the ocean, PV mixing occurs at boundaries, either those of the eddy or those of the ocean (surface, bottom, inflows/outflows). Previous studies of PV dynamics have quantified the effects of forcing and mixing processes on the PV distribution (Marshall et al., 1999, 2012). Although PV is an Eulerian criterion that can vary under changing boundary conditions, it remains a powerful tool for studying ocean dynamics.

In this paper we provide a first answer to some of these questions, focusing on eddies sampled with relatively good resolution (O(20km) horizontally and O(10m) vertically) during cruises in nine different regions. The goal is to characterize the 3D structure of the sampled eddies in order to assess their material coherence. For eddies, the thermohaline properties of their core are conserved during their lifetime. Therefore, by computing thermohaline anomalies on isopycnals, the difference in thermohaline properties between eddy cores and their surroundings can be highlighted and the material coherence can be assessed. However, using in situ data, material coherence is only assessed at a given time. Then, for each eddy, the internal anomaly is correlated with its surface signature revealed by altimetry. For eddies that have been found to be materially coherent, we propose two methods for the extrapolation of their transport volume from a single section sampling its properties at depth. Finally, we compare several criteria to determine their boundaries: thermohaline anomalies, Ertel PV, and relative vorticity. We also use a newly proposed criterion based on Ertel PV (see Barabinot et al. (2024)).

The paper is organized as follows. Section 2 describes the set of *in situ* data used and the identification of eddies using ship-based or satellite altimetry data. Section 3 presents the diagnostics used to characterize the core and boundary of mesoscale eddies and links them to MC definitions. In particular, a section is devoted to the relative errors in the data that affect the accuracy of the results. Then, assuming the circularity or ellipticity of a sampled eddy, two methods are proposed to reconstruct its 3D structure. In section 4 we discuss the material coherence of sampled eddies and in section 5 we present results on volume approximations.

2 Data collection and processing

2.1 Data collection: cruises

The data analyzed here were collected during 9 oceanographic cruises in 7 different regions: the EUREC^{4}A-OA campaign along the northern coast of Brazil, which studied mesoscale eddies and the ocean-atmosphere coupling; the MARIA S. MERIAN MSM60 expedition, which was the first basin-wide section across the South Atlantic following the SAMBA/SAMOC line at 34°30'S; the PHYSINDIEN 2011 experiment along the Omani coast (western Arabian Sea), which studied the eddy field in this area; the FS METEOR M124 expedition, which was the first of the two SACross2016 expeditions; the MSM74 cruise, which was dedicated to determining the intensity of southward water mass transport and transformation in the boundary current systems off Labrador; the M160 measurements, which contributed to the understanding of the ocean eddies generated in the Canary Current system; and three cruises - KB 2017606, KB 2017618, HM 2016611 - whose main objective was to study eddy dynamics in the Lofoten Basin. The goal was to collect a relatively large number of eddies sampled in different regions at different times of their life cycle. To be able to derive our diagnoses from the data, the campaigns must not only have carried out hydrological measurements, but also velocity measurements over the same depth range. This requirement significantly reduces the number of potentially available cruises. The table 1 summarizes the basic information about the cruises:

Table 1. Basic information about the cruises: date, main ocean basin where the campaign took place, sampling instruments used in this paper (it does not refer to every instrument used during cruises).

Name	date	location	Instruments
EUREC4A-OA	20/01/2022-20/02/2020	North Brazil	CTD/uCTD/XBT/sADCP
MSM60	4/01/2017-1/02/2017	SAMBA/SAMOC line ($34°30'S$)	CTD/lADCP (38kHz)
PHY11	03/2011	Red sea, Persian Gulf	Seasor/xCTD /VM ADCP (38kHz)
M124	29/02/2016 - 18/03/2016	South Atlantic	uCTD/XBT /lADCP (38kHz)
MSM74	25/05/2018 - 26/06/2018	Labrador Basin	CTD /SADCP (75kHz)
M160	23/09/2019 - 20/12/2019	Canary	CTD / lADCP (75kHz)
HM2016611	26/05/2016 - 15/06/2016	Lofoten Basin	CTD /lADCP (38kHz)
KB2017606	10/03/2017 - 23/03/2017	Lofoten Basin	CTD /lADCP (38kHz)
KB2017618	02/09/2017 - 15/09/2017	Lofoten Basin	CTD /lADCP (38kHz)

Here, we recall the measurement uncertainties depending on the instrument used. They will be important for estimating errors in the calculated diagnostics. For the CTD instrument, temperature and salinity are measured with uncertainties of $\pm 0.002°$C and ± 0.005psu respectively. For the uCTD instrument, the uncertainties are $\pm 0.01°$C and ± 0.02psu for temperature and salinity measurements respectively. And for the ADCP instrument, the horizontal velocity is typically measured with an uncertainty of ± 3cm/s.

2.2 Data processing

Oceanographic research cruises often collect data along vertical sections that include vertical profiles. Therefore, we define the resolution of a vertical section as the average of all distances between successive profiles along the same section. Since hydrological and velocity instruments do not sample the ocean with the same resolution, the two types of measurements are distinguished (see table 2). For example, the hydrological properties of the surface anticyclonic eddy from EUREC4A-OA (denoted $N°1$ in Table 2) were sampled using CTD/uCTD instruments with a resolution of 3.5km horizontally and 1m vertically, while its dynamical properties were measured using sADCP (75kHz) instruments with a resolution of $>$ 1km horizontally and 8m vertically.

The raw data were calibrated and then interpolated. To limit noise, linear interpolations were performed in $\vec{x}$ (horizontal) and $\vec{z}$ (vertical) directions. We chose first-order polynomial functions to avoid creating artificial fields. The typical grid size of the interpolated data is 1km horizontally and 1m vertically. The data were then smoothed with a numerical low-pass filter of order 4 (scipy.signal.filt in Python). The choice of cut-offs is subjective and depends on the scales considered. Here we are considering mesoscale eddies, so we chose $L_x \geq$ 10km and $L_z \geq$ 10m for the horizontal and vertical length scales where possible to remove submesoscale processes that can blur eddy boundaries. In fact, the cut-off period must be longer than the sampling resolution of the calibrated data. The smoothing parameters are summarized in Table 2.

2.3 Eddy identification in cruise data

Since on vertical density sections the rotational dynamics mainly satisfy the geostrophic equilibrium with often a small cyclostrophic correction (Cushman-Roisin, 1994; Penven et al., 2014; Ioannou et al., 2019), eddies can be identified by observing vertical deviations of isopycnals; they are usually accompanied by changes in the sign of the velocity field orthogonal to the section. To analyze the true thermohaline anomalies in eddy cores, the ship must have passed close enough to the eddy center. In the following, we separate such sampled eddies from others. We call R_{max} the radius of maximum velocity if the eddy is axisymmetric, and e the distance between the eddy center and its orthogonal projection on the ship's track (see figure 1). An eddy is considered well sampled if $e \leq R_{max}/2$. Obviously, eddies are not completely axisymmetric and we adjust the criterion for this case using L as defined in figure 1. Using the Pythagorean theorem, an eddy is well sampled if the following condition is satisfied: $e \leq L/\sqrt{3}$. Table 3 summarizes the basic properties of eddies and describes which eddies are well-sampled.

The position of the eddy center is estimated using the routine from Nencioli et al. (2008) at the depth of the observed maximum velocity, assuming that the position of the center does not vary too much with depth. The routine constructs a rectangular area around the ship track with a given grid size. Then, for each grid point, the distance-weighted average of the tangential velocity is computed using each velocity vector measured along the transect. The center of the eddy is defined as the point where the mean tangential velocity is maximum.

Finally, we are able to locate every well-sampled eddy during the 9 cruises. In practice, however, some non-well-sampled eddies have sufficient characteristics to assess their material coherence. In total, 26 eddies (18 anticyclonic eddies and 8 cyclonic eddies) were sampled, including 19 well-sampled eddies (12 anticyclonic eddies and 7 cyclonic eddies). Therefore, some biases have to be pointed out: more anticyclonic (AC) eddies were sampled than cyclonic (C) eddies, the eddies studied come from only 7 specific regions, which is not representative for all eddies in the global ocean, and of course the eddies were sampled during their drift, leaving uncertainties in the results.

Table 2. Cruise names, type, and resolution of the 26 mesoscale eddies studied. The resolution of the hydrographic data is denoted by Δ_H, while the velocity data is denoted by Δ_V. For each type of data, the horizontal and vertical resolutions are explained, as well as the cutoff of the low-pass filter used to smooth the data. Some eddies have the same horizontal resolution when sampled along the same transect. The variation in resolution for eddies on the same transect is negligible. AC = anticyclonic eddy, C = cyclonic eddy, surf = surface eddy, sub = subsurface eddy.

$N°$	Cruise	Type	$\Delta_H x$ (L_x) [km]	$\Delta_H z$ (L_z) [m]	$\Delta_V x$ (L_x) [km]	$\Delta_V z$ (L_z) [m]
1	EUREC4A-OA	AC KSurf/**TSub**	3.5 (10)	0.5 (10)	0.3 (10)	8 (10)
2	EUREC4A-OA	AC KSub/TSub	8.4 (10)	0.5 (10)	0.3 (10)	8 (10)
3	EUREC4A-OA	AC KSub/TSub	13 (15)	0.5 (10)	0.3 (10)	8 (10)
4	MSM60	C KSurf/TSub	26.3 (50)	1 (10)	26.3 (50)	8 (10)
5	MSM60	C KSurf/TSub	41.7 (50)	1 (10)	41.7 (50)	8 (10)
6	MSM60	C KSurf	43 (50)	1 (10)	43 (50)	8 (10)
7	PHY11	AC KSurf/TSub	1.8 (10)	0.1 (10)	0.3 (10)	8 (10)
8	PHY11	AC KSub/TSub	1.7 (10)	0.1 (10)	0.3 (10)	8 (10)
9	M124	C KSurf/TSub	25 (30)	0.5 (10)	0.3 (10)	32 (40)
10	M124	AC KSurf/TSub	23 (30)	0.5 (10)	0.3 (10)	32 (40)
11	M124	AC KSurf/TSub	23 (30)	0.5 (10)	0.3 (10)	32 (40)
12	M124	AC KSub/TSub	23 (30)	0.5 (10)	0.3 (10)	32 (40)
13	M124	AC KSub/TSub	12 (30)	0.5 (10)	0.3 (10)	32 (40)
14	M124	AC KSub/TSub	21 (30)	0.5 (10)	0.3 (10)	32 (40)
15	M124	AC KSub/TSub	21 (30)	0.5 (10)	0.3 (10)	32 (40)
16	M124	AC KSub/TSub	20 (30)	0.5 (10)	0.3 (10)	32 (40)
17	M124	AC KSub/TSub	20 (30)	0.5 (10)	0.3 (10)	32 (40)
18	MSM74	AC KSurf/TSub	35.7 (40)	1 (10)	0.3 (10)	8 (10)
19	MSM74	C KSurf/TSub	33.5 (40)	1 (10)	0.3 (10)	8 (10)
20	MSM74	C KSurf/TSub	33.5 (40)	1 (10)	0.3 (10)	8 (10)
21	MSM74	C KSurf	20.3 (30)	1 (10)	0.3 (10)	8 (10)
22	MSM74	AC KSurf	20.3 (30)	1 (10)	0.3 (10)	8 (10)
23	m160	C KSurf	15.1 (20)	1 (10)	0.3 (10)	8 (10)
24	KB2017606	AC KSub/TSub	6.6 (10)	1 (10)	6.6 (10)	8 (10)
25	KB2017606	AC KSub/TSub	5.3 (10)	1 (10)	5.3 (10)	8 (10)
26	HM2016611	AC KSub/TSub	5.8 (10)	1 (10)	5.8 (10)	8 (10)

Here we specify the determination of the eddy type. On the one hand, the cyclonic or anticyclonic aspect is derived from the deviation of the isopycnals: On the other hand, the surface or subsurface intensification of the vortex depends on the variable used to characterize its vertical structure. Thus, two variables can be used: the location of the maximum velocity and the location of the maximum thermohaline anomalies (defined later by Eqs. (1) and (2)). A kinematic subsurface eddy (KSub) is defined as an eddy for which the maximum velocity is below -70m depth. Conversely, a kinematic surface eddy (KSurf) has its maximum velocity in the upper -70m depth. A thermohaline subsurface eddy (TSub) is an eddy for which the maximum of the thermohaline anomalies on isopycnals (see separate section) is below -70m depth. In contrast, thermohaline surface eddies (TSurf) have their maximum anomalies defined within this upper layer. In

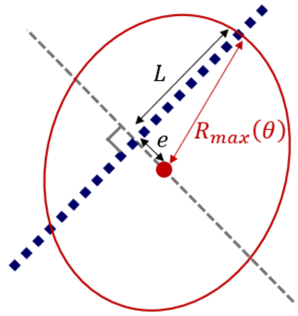

Figure 1. A schematic example of a well-sampled eddy at the sea surface: the red dot indicates the estimated center; the dark blue squares are locations of vertical profiles; the red circle is the radius of maximum tangential velocity. The dashed gray line is perpendicular to the ship track passing the eddy center.

fact, ADCP data are only accurate after 2 or 3 bins of depth. Some cruises do not even provide data in the first $-50m$. In addition, isopycnal levels must match between the section and the climatological mean, which is rarely satisfied near the surface due to near-surface variability. As a result, it is often impossible to calculate anomalies above −70m. Therefore, the −70m depth threshold has been chosen to have a unique value regardless of the variable being considered. In some cases, eddies are not materially coherent and no maximum of anomalies can be found at the center of the eddy (see part 5.1). Therefore, only the velocity is used to assess the vertical structure. In the literature, when an eddy is labeled KSurf, it is also labeled TSurf (same for Ksub). This is not the case here.

2.4 Satellite altimetry data and the TOEddies algorithm

To confront the surface and subsurface signature of sampled eddies, we present satellite altimetry data and a detection algorithm based on Absolute Dynamical Topography derived from these data.

Sampled eddies are identified and tracked in time by the TOEddies automatic detection algorithm (Laxenaire et al., 2018, 2019, 2020). This detection is applied to adhoc Near Real Time (NRT) ADT maps during the field experiments. These products are provided by Collecte Localization Satellites (CLS) and have been generated using a Mean Dynamic Topography (MDT) with a higher resolution (1/8° instead of 1/4°) than the standard MDT product.

The TOEddies method is based on the algorithm proposed and developed by (Chaigneau et al., 2009) and has already been used in studies analyzing different aspects of Atlantic Ocean dynamics, such as the origin and evolution of the Agulhas Current rings (Laxenaire et al., 2018, 2019, 2020), the role of mesoscale eddies in meridional transport over the zonal South Atlantic GO-SHIP section of the MSM60 cruise (Manta et al., 2021), in the EUREC4A-OA region (Subirade et al., 2023), and the effect of mesoscale eddies on the formation and transport of South Atlantic subtropical mode water (Y. Chen et al., 2022).

Assuming that eddies are in geostrophic equilibrium, TOEddies identifies eddies as closed contours of the ADT that include only a local extremum. As a result, the instantaneous eddy streamlines should coincide with the closed isolines of the daily ADT maps. Thus, ADT, and not SLA, represents the geostrophic stream function. In fact, SLA is very sensitive to large SSH gradients associated with intense currents and quasi-stationary meanders or eddies that characterize the MDT (see example in Pegliasco et

Table 3. Basic properties of mesoscale eddies: typical variation of isopycnal deviation (H is an order of magnitude here); radius of maximum velocity on the vertical section ($L \neq R_{max}$ of figure 1); maximum velocity (V_m) associated with L; apparent Rossby number $R_o = V_m/(f_0 L)$. Since mesoscale eddies are not axisymmetric, V_m is taken as the maximum modulus of V_o, the velocity component orthogonal to the ship section. The "Well-sampled" column indicates whether the eddy is well-sampled (Yes) or not (No). The "Complete" column indicates whether the eddy has been completely sampled. The letters [C/B/H] mean [Complete/Boundary/Half]: "Complete" if the eddy structure is clearly visible on vertical sections, a "+" is added if vertical boundaries are visible, "Boundary" if only one boundary is visible, and "Half" if one boundary plus the center is visible. The center refers to the location where the velocity V_o is zero. If only half of the vortex structure has been sampled, the Nencioli et al. (2008) routine cannot be applied, so we enter "-". In fact, this table underscores the difficulty of obtaining complete (all boundaries visible) well-sampled structures with *in situ* data. For a mesoscale eddy marked "B", the eddy radius cannot be calculated and dashes are used. Note that the radius L has also been estimated for nonwell-sampled eddies.

$N°$	Cruise	type	H[m]	L[km]	V_m[m/s]	R_o	Well-sampled	Complete [C/H/B]
1	EUREC4A-OA	AC	70	121	1.14	0.44	Yes	C+
2	EUREC4A-OA	AC	220	71	0.96	0.61	Yes	C+
3	EUREC4A-OA	AC	115	111	0.83	0.32	Yes	C+
4	MSM60	C	375	85	0.6	0.11	Yes	C+
5	MSM60	C	190	42	0.33	0.10	Yes	C
6	MSM60	C	170	28	0.6	0.26	Yes	C
7	PHY11	AC	55	95	0.99	0.38	Yes	C+
8	PHY11	AC	20	10	0.36	0.66	Yes	C+
9	M124	C	120	67	1.53	0.28	Yes	C
10	M124	AC	200	58	1.27	0.26	Yes	H
11	M124	AC	105	55	0.95	0.21	Yes	C
12	M124	AC	-	-	-	-	-	B
13	M124	AC	130	54	0.75	0.19	Yes	C
14	M124	AC	40	34	0.32	0.13	No	C
15	M124	AC	30	52	0.32	0.08	No	C
16	M124	AC	-	-	-	-	-	H
17	M124	AC	150	61	0.73	0.16	Yes	C
18	MSM74	AC	180	28	0.23	0.06	Yes	C
19	MSM74	C	100	35	0.17	0.04	No	C
20	MSM74	C	100	32	0.43	0.1	Yes	C
21	MSM74	C	150	23	0.24	0.04	Yes	C
22	MSM74	AC	150	12	0.3	0.2	Yes	C
23	m160	C	50	49	0.46	0.09	Yes	C
24	KB2017606	AC	-	-	-	-	-	B
25	KB2017606	AC	500	15	0.78	0.34	Yes	C+
26	HM2016611	AC	-	-	-	-	-	B

al. (2021)). TOEddies thus identifies the local ADT extrema (maxima and minima) and searches for the outermost closed ADT contour around each extremum. In addition to the outermost closed ADT contour, TOEddies also identifies the contour where the mean azimuthal velocity is maximum using geostrophic velocities derived from ADT maps.

3 Methods for eddy boundaries characterization

3.1 Thermohaline anomalies on isopycnals surfaces

The ability of eddies to trap and transport water masses is the basis of the MC definition. Here, we evaluate this definition by computing temperature and salinity anomalies on isopycnals in eddy cores relative to a climatological average following the method of Laxenaire et al. (2019, 2020). The climatological average of temperature/salinity on geopotential levels is calculated using ARGO float profiles over 20 years in a small area around the sampled eddy. The Coriolis dataselection.euro-argo.eu database is used. A square of side 0.5° is built around the eddy center estimate, so that the center is at the intersection of the diagonals. Taking T^* and S^* as two reference profiles in temperature and salinity (outside the eddies) and T and S as *in situ* profiles (inside the eddies), thermohaline anomalies on isopycnals are computed as follows:

$$\forall\sigma_0, \quad \Delta T(\sigma_0) = T(\sigma_0) - T^*(\sigma_0) \tag{1}$$

$$\forall\sigma_0, \quad \Delta S(\sigma_0) = S(\sigma_0) - S^*(\sigma_0) \tag{2}$$

where σ_0 is the potential density at atmospheric pressure. These anomalies are computed on isopycnal surfaces but interpolated to the geopotential level to facilitate comparison with other criteria. As introduced earlier, we define a thermohaline subsurface eddy (TSub) as an eddy with an anomaly maximum deeper than 70m. Conversely, a thermohaline surface eddy (TSurf) has its anomaly maximum above 70m depth. These anomalies can separate two water masses that have the same potential density but different thermohaline compositions. They are therefore very powerful in delineating the materially coherent core of an eddy. Taking into account the resolution of the instruments, the uncertainty in the thermal (or salinity) anomalies is about ±0.01°C (±0.02psu) for sections where uCTD has been used, and ±0.002°C (±0.005psu) where only CTD measurements have been made.

These anomalies are highly dependent on the temperature or salinity gradient along the isopycnals. This criterion may have limitations in regions where the density is only driven by temperature (or salinity). In our case, we only consider eddies sampled at mid-latitudes, where both salinity and temperature drive the stratification.

3.2 Gradients

Since the Taylor expansion was truncated, the second order terms $\frac{(\Delta x)^2}{2}\frac{\partial^2 a}{\partial x^2}$ have been neglected with respect to those of order one $\Delta x\frac{\partial a}{\partial x}$. An approximation of these second order terms for the temperature, salinity, and velocity fields has been calculated to substantiate this point. For example, using data from the EUREC^{4}A-OA cruise, the second-order terms for temperature average about $1.10^{-6^\circ}C/m$ horizontally and $0.6.10^{-4^\circ}C/m$ vertically. These values are small compared to the first-order terms ($7.6.10^{-6^\circ}C/m$ horizontally and $2.5.10^{-2^\circ}C/m$ vertically). For temperature, the second-order terms are thus 13% of the first-order terms horizontally and 0.03% vertically. For salinity and orthogonal velocity, the horizontal (vertical) first-order terms are larger than the second-order terms by factors of 10 (10^2) and 10^2 (10^3), respectively. With these approximations, the gradients of the various fields can be calculated reliably.

For a given quantity a, the norm of a gradient in a 2D slice is defined as follows

$$|\vec{\nabla} a| = \sqrt{\left(\frac{\partial a}{\partial x}\right)^2 + \left(\frac{\partial a}{\partial z}\right)^2} \tag{3}$$

As an eddy locally modifies isothermals or isohalines with respect to the state of rest, we expect this quantity be useful to detect eddies boundaries.

We also defined the Brunt-Väisälä frequency as:

$$N^2 = \frac{-g}{\sigma_0^{(0)}} \frac{\partial \sigma_0}{\partial z} \tag{4}$$

where $\sigma_0^{(0)}$ is a reference value averaged over each profile of the section and g is gravity. Since the eddy properties deviate from those of the background environment along the isopycnal surfaces, they are actually stratification anomalies. As such, the core appears as a region of low (or high) gradients for AC (or C).

To calculate the relative vorticity, derivatives in two different horizontal directions are needed. For a single section from a research cruise, this is not possible without further assumptions. An approximation of the relative vorticity is the "Poor Man's Vorticity" (PMV) introduced by Halle and Pinkel (2003). It decomposes the measured velocities into a cross-track component $v_\perp$ and an along-track component $v_\parallel$. The relative vorticity is then approximated as $\zeta_z \approx 2\frac{\partial v_\perp}{\partial x}$. The factor 2 is added so that the PMV is equal to the actual ζ in an eddy core with solid body rotation. However, Rudnick (2001); Shcherbina et al. (2013) used the along track derivative of the cross track velocities without the factor 2. Both approximations differ only in the way they estimate the cross-track derivative of the along track velocities. This method can be criticised and other approximations can be found in the literature. In this article we arbitrarily choose the 2D approximation of Rudnick (2001):

$$\zeta_z \approx \frac{\partial v_\perp}{\partial x} \tag{5}$$

Unless otherwise stated, the velocity field is always perpendicular to the section plane. Relative vorticity has been used extensively in studies based on analyses of satellite altimetry data to calculate the eddy volume. Some Lagrangian criteria such as LADV (Lagrangian-averaged vorticity deviation) are also based on this quantity and are therefore of interest.

3.3 Ertel Potential Vorticity (EPV)

Here the 3D formula of EPV (Ertel, 1942) is simplified and applied to *in situ* data. Under the Boussinesq approximation and hydrostatic equilibrium, the vertical velocity vanishes. We denote it as $1/\sigma_0 \approx 1/\sigma_0^{(0)}$. Therefore, following the method of Pierre et al. (2016), the EPV for a 2D vertical section has the following form

$$EPV = EPV_x + EPV_z = -\frac{\partial V_o}{\partial z}\frac{\partial b}{\partial x} + (\zeta_z + f)\frac{\partial b}{\partial z} \tag{6}$$

where $b = -g\frac{\sigma_0}{\sigma_0^{(0)}}$ is the buoyancy, V_o is the velocity component orthogonal to the section plane, and ζ_z is as defined above. Note that this expression only gives a 2D approximation of the real EPV with a baroclinic term EPV_x and a term involving the rotating flow and stretching EPV_z. Therefore, the EPV of the ocean at rest (hereafter $\overline{EPV}$) is

$$\overline{EPV} = f\frac{d\bar{b}}{dz} \tag{7}$$

where $\bar{b}$ is the climatological reference profile in the area of the eddy. The *Ertel Potential Vorticity Anomaly* is then calculated on density surfaces (i.e. using density as the vertical coordinate) as follows:

$$\Delta EPV \quad = \quad EPV_x + \Delta EPV_z \tag{8}$$

$$\Delta EPV_z = EPV_z - \overline{EPV} \quad (9)$$

$$\forall \sigma_0, \quad \Delta EPV(\sigma_0) = EPV(\sigma_0) - \overline{EPV}(\sigma_0) \quad (10)$$

As for thermohaline anomalies, this quantity is calculated on isopycnic surfaces and then represented on geopotential levels. This quantity has been widely used to define the materially coherent core of eddies and is therefore of interest (Zhang et al., 2014).

Following the approach of Barabinot et al. (2024), we also defined the ratio between the anomaly of the vertical component ΔEPV_z and the horizontal one EPV_x: $\Delta EPV_z/EPV_x$. In fact, it was shown that the eddy boundary is not locally defined and behaves like a frontal region subject to symmetric instabilities. These instabilities occur when the baroclinic term becomes non-negligible in front of the vertical term (Hoskins, 1974; Hoskins & Bretherton, 1972). Consequently, a criterion of the type:

$$\frac{\Delta EPV_z}{EPV_x} > \beta \quad (11)$$

with $\beta \gg 1$ will detect the core water that is not in the turbulent frontal region. Symmetric instabilities can erode the core by changing the properties of the water parcels at the boundaries or by generating small scale turbulence (Thomas et al., 2016; D'asaro et al., 2011; Haine & Marshall, 1998; Goldsworth et al., 2021). This detected water is more stable and is subject to drift with the eddy without being altered by the environment.

3.4 Comparison between criteria

Which of these criteria is most effective in detecting the materially coherent core? Some criteria have already been studied by Barabinot et al. (2024). They showed that the eddy core is surrounded by a turbulent region subject to instabilities characterized by a value of $\frac{EPV_x}{EPV_z}$ close to 1. Consequently, the largest values of the ratio $\frac{\Delta EPV_z}{EPV_x}$ define the eddy core, which is less subject to instabilities and where the trapped water is less likely to be mixed and modified by the environment. By superimposing the thermal anomaly and the $\frac{\Delta EPV_z}{EPV_x}$ contours, we determine the materially coherent core, which should undergo little change in properties during the eddy drift. However, this criterion must be applied to the eddy core where the heterogeneous water is retained.

To capture the true materially coherent core of an eddy, two criteria must be used. First, thermohaline anomalies on isopycnal surfaces must be computed to detect the region where the trapped water is located. The outermost closed contour is used to bound an approximate core. However, the boundary provided by thermohaline anomalies is only a line. But some water in its vicinity may cross it and escape the core due to instabilities. Therefore, the $\frac{\Delta EPV_z}{EPV_x}$ criterion is used within the first region to remove the boundary region subject to instabilities. The last region is much more restrictive, but represents the stable confined water inside the core.

Ertel Potential Vorticity combines the stratification anomaly, the rotating flow, and the influence of the Earth's rotation. As a result, the boundaries determined by the thermohaline anomalies on isopycnals, the relative vorticity, and the buoyancy frequency drive those determined by Ertel Potential Vorticity.

In practice, it is difficult to apply the $\frac{\Delta EPV_z}{EPV_x}$ criterion to *in-situ* data because it requires high resolution data due to multiple derivations and is quite sensitive to noise. We now show that this criterion can be theoretically approximated by the buoyancy frequency.

In the region where $\frac{EPV_z}{EPV_x} \gg 1$, we have

$$EPV = (\zeta_z + f_0)\frac{\partial b}{\partial z} \tag{12}$$

Using scales: B for b, V for v_θ, R for r, this dimensionless quantity (marked with a hat) becomes

$$E\hat{P}V = (\hat{\zeta_z} + \frac{1}{Ro})\frac{\partial \hat{b}}{\partial \hat{z}} \tag{13}$$

where $Ro = V/(f_0 R)$ is the Rossby number for an axisymmetric vortex. For mesoscale eddies, $Ro < 1$ and even $Ro \ll 1$. So the relative vorticity is negligible. Thus

$$E\hat{P}V = \frac{1}{Ro}\frac{\partial \hat{b}}{\partial \hat{z}} \tag{14}$$

Therefore, the buoyancy frequency is a good proxy for our criterion. Note that $f_0\frac{\partial b}{\partial z}$ has already been considered as a PV anomaly by previous studies (Paillet, 1999; Paillet et al., 2002).

3.5 Uncertainties/Relative Errors

Since the gradients are calculated using the finite difference method, the error can be estimated. For example, given the horizontal gradient of the temperature $\partial_x T$ of a given velocity profile and resolution, the error is written as follows

$$\frac{\delta(\partial_x T)}{\partial_x T} = \frac{\delta_H T}{T} + \frac{\delta_H(dx)}{dx} \tag{15}$$

where $\delta_H T$ and $\delta_H(dx)$ refer to the uncertainty in temperature and horizontal resolution, respectively. This formula is obtained by the uncertainty propagation equation in the worst case where there is an inverse correlation between the variables. To get an order of magnitude for this error, we can choose the mean value $T^{(0)}$ for T in the section and the radius of maximum velocity L for the horizontal scale. Here δ_H refers to hydrological data: the horizontal resolution is that of the hydrological gauges. Similarly, δ_V refers to the uncertainty associated with the velocity data.

A similar approach can be used to estimate the errors on gradients of other quantities as well as vertical gradients. For the latter, the typical length scale for z is taken as the maximum isopycnal deviation with respect to the resting stratification. As an example, we compute the uncertainty in EPV_x. Following this approach we write

$$\begin{aligned}
\frac{\delta(EPV_x)}{EPV_x} &= \frac{\delta_H b}{b} + \frac{\delta_H(dx)}{dx} + \frac{\delta_V V_o}{V_o} + \frac{\delta_V(dz)}{dz} && (16)\\
&\approx \frac{\delta_H b}{b^{(0)}} + \frac{\Delta_H x}{L} + \frac{\delta_V V_o}{V_m} + \frac{\Delta_V z}{H} && (17)
\end{aligned}$$

where $\Delta_H x$ is the horizontal resolution of the hydrographic data, $\Delta_V z$ is the vertical resolution of the velocity data (defined in Table 1), $\delta_V V_o$ is the uncertainty in the velocity measurements, $\delta_H b$ is the uncertainty in the buoyancy. For buoyancy, the linearized equation of state was used to determine the uncertainty:

$$\delta_H b = -\frac{g}{\sigma_0^{(0)}}\delta\sigma_0 = -\frac{g}{\sigma_0^{(0)}}(-\alpha\delta_H T + \beta\delta_H S) \tag{18}$$

where g is gravity, $\sigma_0^{(0)}$ is a reference value taken here as an average over each profile of a considered section, $\alpha = 2\times10^{-4}K^{-1}$ and $\beta = 7.4\times10^{-4}g/kg$ are classical averages to simplify the calculation. In fact, due to the small uncertainty in the thermal and salinity fields, the relative uncertainty in the buoyancy $\delta_H b/b$ is often less than 0.1%.

Table 4. Lists of uncertainties for horizontal and vertical gradients of temperature and salinity, relative vorticity and both components of Ertel potential vorticity for a 2D vertical section. Typical quantities useful in the calculation such as $T^{(0)}$ or $S^{(0)}$ are taken as averages over each vertical profile of the vertical section considered.

$N°$	$\frac{\delta(\partial_x T)}{\partial_x T}$ [%]	$\frac{\delta(\partial_z T)}{\partial_z T}$ [%]	$\frac{\delta(\partial_x S)}{\partial_x S}$ [%]	$\frac{\delta(\partial_z S)}{\partial_z S}$ [%]	$\frac{\delta(\partial_z V_o)}{\partial_z V_o}$ [%]	$\frac{\delta\zeta}{\zeta}$ [%]	$\frac{\delta(EPV_z)}{EPV_z}$ [%]	$\frac{\delta(EPV_x)}{EPV_x}$ [%]
1	2.9	11.5	2.9	11.5	14.1	2.9	3.6	17.0
2	11.9	3.7	11.9	3.7	6.8	3.5	3.8	18.6
3	11.8	7.0	11.8	7.0	10.6	3.9	4.3	22.3
4	31.0	2.7	31.0	2.7	7.7	35.9	36.2	38.6
5	99.3	5.3	99.3	5.3	14.4	108	109	114
6	153.6	5.9	153.9	5.9	10.9	158	159	164
7	1.9	14.6	1.9	14.6	17.6	3.3	3.5	19.5
8	17.0	26.7	17.0	26.7	35	11.3	11.7	52
9	31.1	26.7	31.1	26.7	28.6	2.4	2.8	59.7
10	40.0	16.0	40.0	16.0	18.4	2.9	3.1	58.0
11	41.8	30.5	41.8	30.5	33.6	3.7	4.2	75.5
12	-	-	-	-	-	-	-	-
13	22.1	24.6	22.1	24.6	28.6	4.6	4.9	50.8
14	61.8	80.0	61.8	80.0	89	10.3	11.5	151
15	40.4	107	40.4	107	116	10.0	11.6	156
16	-	-	-	-	-	-	-	-
17	32.8	21.3	32.8	21.3	25.4	4.6	4.9	58.2
18	89.3	4.5	89.3	4.5	17.5	13.4	14.0	106.8
19	95.8	8.0	95.8	8.0	25.6	17.9	18.9	121
20	63.5	8.0	63.5	8.0	15.0	7.3	8.3	78
21	88.3	5.3	88.3	5.3	17.8	12.9	13.6	106
22	125.9	5.3	125.9	5.3	15.3	10.8	11.5	141
23	13.5	16.0	13.5	16.0	22.5	20.0	22.0	36.0
24	-	-	-	-	-	-	-	-
25	56.7	1.6	56.7	1.6	5.4	60.5	60.7	62.1
26	-	-	-	-	-	-	-	-

Lists of relative errors for the calculated quantities are given in Table 4. In a few cases, the horizontal resolution of the hydrographic data (CTD or uCTD) is greater than the radius of the maximum eddy velocity provided by the ADCP data, resulting in uncertainties greater than 100%. The accuracy of our gradient calculations is limited by the resolution of the 2D vertical sections. The horizontal resolution of the hydrographic data and the vertical velocity gradient are the most critical parameters. This is well illustrated by the first and last columns, where the uncertainty in EPV_x reaches very high values due to the horizontal buoyancy gradient and the vertical velocity gradient. This can have important consequences at the boundary of an eddy where EPV_x is increasing. On the contrary, due to the high horizontal resolution of the ADCP data, the uncertainties on the relative vorticity and EPV_z are limited and mostly remain below 20%.

4 Methods to compute eddies volume

There are many methods in the literature to approximate and calculate mesoscale eddy volumes. This step is crucial for estimating tracer transport by these structures. For example, some altimetric studies have used cylinders to approximate eddy cores even when the true vertical structure is unknown. Lagrangian studies are also very powerful to estimate tracer transport using Lagrangian criteria such as LADV (Hadjighasem et al., 2017). However, as mentioned in the introduction, many of these studies used only altimetric data, which are not suitable to rigorously estimate eddy volumes because they only consider geostrophic surface currents. In fact, there is neither a consensus on the shape of eddies nor a rigorous method to compute their volume. In this section, we describe two reconstruction methods to estimate eddy volumes from a single ship section.

4.1 Basic Considerations

Consider an eddy whose boundaries are defined by a criterion (a given isoline of temperature/salinity anomaly, EPV, gradients, etc., see Barabinot et al. (2024)). This eddy was sampled by a ship transect that does not necessarily cross the exact eddy center, defined as the location of the zero velocity. Therefore, the difference between the exact eddy center and the center on the resulting 2D section will affect the reconstruction of the 3D structure and thus the volume.

To illustrate this fact, consider a perfect cylindrical vortex core with radius R and height H. We assume that it is located at the ocean surface and that it has been sampled by a ship track as shown in Figure 1, so that L appears as the eddy radius on the 2D vertical section. An estimate by a simple calculation of the eddy volume using this 2D vertical section gives a volume of $\pi L^2 H$, which has to be compared with the real volume of $\pi R^2 H$. Using the Pythagorean theorem, it can be shown that the relative error, expressed as a fraction of the exact volume, is $\frac{e^2}{2R^2}$, assuming $e \ll R$. The relative error is less than 5% if $e \leq \frac{R}{\sqrt{10}} \approx 0.316R$. In this case, e must be less than 31.6% of R for this condition to be true. This condition is not really restrictive, and the reconstruction can be quite faithful.

If we now assume that the eddy is cone-shaped with a base of radius R and height H, the relative error is different. Assuming that the eddy has been scanned by a ship's track, as in figure 1, the boundary of the eddy will appear as a hyperbola of maximum height H_e on the 2D vertical section. Now the eddy will appear less deep than it is in reality. The relative error between the exact and reconstructed volumes will be $3\frac{e}{R}$. This result follows only from basic geometric considerations (see figure 2). In this case, for the relative error to be less than 5%, e must be less than 1.7% of the eddy radius, which is very restrictive. Given the horizontal resolution of the data, and thus the uncertainty in the radius, the reconstruction method will be highly inaccurate.

Therefore, depending on the shape of the eddy, the distance between the ship track and the eddy center e is a critical parameter and strongly influences the uncertainty of the volume approximations. To reduce this uncertainty, volumes are computed only for eddies with a very small value of e. In our database, only 4 eddies ($N°1, 2, 7, 26$) have been sampled by a ship track crossing the eddy within a very small distance from its center ($e < 3km$) and can thus be used to compute volumes.

Different volumes can be studied analytically, and the same approach can be followed for subsurface eddies. As shown in previous studies, surface eddies appear to have shapes close to cylindrical or conical volumes (not necessarily with a circular basis), but

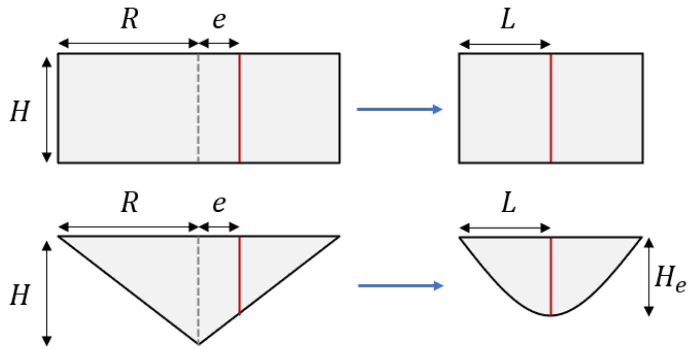

Figure 2. Simple approximation using a ship's cross section: an eddy is a solid of revolution (cylindrical at the top, conical at the bottom). On the left is the real eddy core, bounded by a criterion. On the right, the reconstruction based on the ship section. The dashed gray line is the position of the eddy center, which does not vary, and the red line is the perfectly vertical section. For clarity, only a 2D view is shown, but each volume is axisymmetric.

some approximations exist for subsurface eddies. Some of them assimilated eddies to pancakes because the horizontal scale is much larger than the vertical one (Bars et al., 2011). In reality, however, an eddy has a more complex shape, depending on the criterion used to define its boundaries. It is not perfectly axisymmetric and its center is not perfectly vertical. More precisely, the shape is determined by the rotating flow and depends on the deformation that the vortex undergoes. It can be stretched and sheared by the mean background flow. It has been shown that the flow function of the rotating flow can be decomposed into azimuthal normal modes (Gent & McWilliams, 1986). Depending on the order of the modes, the flow pattern is modified. If the eddies are strongly disturbed, the decomposition of the flow function into normal modes may include high order terms. In most cases, however, three modes dominate: order 0, which corresponds to a purely circular eddy, order 1, which captures the north-south anomaly due to the β effect, and order 2, which corresponds to an elliptical eddy (Carton, 2001; de Marez et al., 2020). In this context, we propose two approaches to approximate the volume (associated with a criterion) of an eddy sampled by a ship section, assuming first mode 0 and then mode 2 are dominant.

Both approaches use the $f-$plane approximation. Both reconstructions are thus performed in a Cartesian space, neglecting the local curvature of the sea surface.

4.2 Reconstruction using cylinders with a circular base

The methodology is illustrated in figure 3. We now reconstruct the 3D structure of an eddy using the same approach as in figure 2, but we take into account its vertical tilt. The eddy remains perfectly circular at each geopotential level, its center being that given by the ship's section. The total volume is the sum of the volumes of the elementary cylinders.

This method allows the variation of the eddy radius with depth and the eccentricity of the eddy center to be preserved. This reconstruction is also relatively simple. However, it assumes that the eddy is perfectly circular at each geopotential level, which is a strict hypothesis. Also, the center is that of the 2D ship section, and the calculation of the volume does not depend on e, although we have shown that it has an influence. To summarize, the approach consists of three steps:

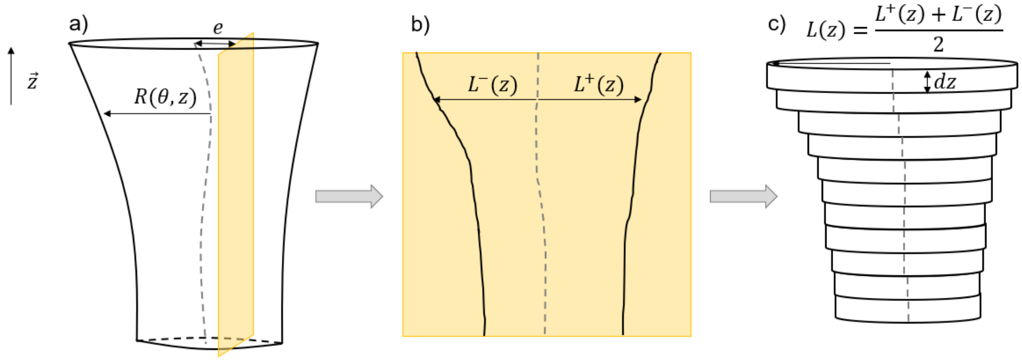

Figure 3. Methodology for reconstructing the 3D structure of an eddy from a single ship track. Here, a surface eddy was used, but the approach also works for a subsurface eddy. a) Real surface eddy, for which the volume is defined by a criterion: the real eddy center is represented by a dashed gray line and the sampled vertical section in yellow. The eddy is not axisymmetric and its radius is a function of the cylindrical variables θ and z. This structure has been sampled by a yellow vertical ship track characterized by the distance e from the real eddy center. b) Vertical section where the boundary is estimated by the same criterion: here the dashed grey line represents an approximation to the real eddy center. To be consistent with the previous notation, the radius of the vortex is denoted L. Since the eddy is not symmetric, we differentiate the radius associated with the positive and negative poles of the velocity field (even if the criterion is not based on velocity). c) The 3D shape of the eddy is reconstructed as an association of infinitesimal cylinders of radius averaged between L^+ and L^- and of small height dz. The total volume can be calculated by summation. The center of each small cylinder is that of the 2D vertical section and thus remains in the plane of the ship section.

1. Select a criterion (the outermost closed contour of a given size) to delimit the materially coherent eddy core from its surroundings on the 2D vertical slice.
2. Compute the position of the apparent eddy center as the location where the orthogonal velocity V_o is zero and the eddy radius $L(z)$ associated with the selected criterion.
3. Calculate the approximate volume as a sum of elementary cylinders.

This method defines the uncertainty due to resolution:

$$\frac{\delta\Omega}{\Omega} = \frac{\int_{-H-\delta(dz)}^{0} \pi(L(z) + \delta(dx))^2 dz - \int_{-H}^{0} \pi L^2(z) dz}{\int_{-H}^{0} \pi L^2(z) dz} \tag{19}$$

where Ω is the approximated volume, $\delta(dx)$ is the horizontal resolution, and $\delta(dz)$ is the vertical resolution (depending on the type of device). This formula is valid for a surface eddy. In the subsurface case, the integral must be replaced by $\int_{-\frac{H+\delta(dz)}{2}}^{\frac{H+\delta(dz)}{2}}$.

4.3 Reconstruction using elliptically based cylinders

Using altimetry data and detection algorithms, G. Chen et al. (2019) showed that ellipses are the most common shape for ocean surface eddies. Perfectly elliptical eddies are rare, but ellipses remain the best fit to characterize the shape of almost the entirety of surface eddies. Indeed, isolated eddies tend to be circular, but in the global ocean, eddies are often deformed by the background flow or its beta drift, and thus undergo elongation. They calculated the best-fit ellipses for eddies over a 20-year period (1996-2016) and analyzed the eccentricity of the eddies that left an imprint on the ocean surface. They also studied the average orientation of the semi-major axis of these elliptical eddies with respect to the parallels in each ocean basin. As a result, they obtained the distribution of the average eccentricity as a function of latitude, as well as the distribution of the average orientation of the semi-major axis (see Figure 6 and 8 from G. Chen et al. (2019)). Although they worked on surface eddies, we assume that their results also apply to subsurface eddies. Here we show how to reconstruct an elliptical eddy using the latter two results and a ship track.

The approach is the same as in the previous part. At each geopotential level within the eddy core, an ellipse is constructed to find an elementary volume of height dz. By summing at each geopotential level, the total volume is obtained. Figure 4 illustrates the main geometric points and constructions used to find the semi-major and semi-major axes of the ellipse. For each geopotential level within the eddy core, the main steps can be described as follows:

1. Using the orthogonal velocity V_o, the eddy center C on the ship section is calculated. With a given criterion, the eddy core boundary is determined and P and Q, the extremities of the core on the ship section, are defined.
2. Using the Nencioli et al. (2008) routine for the considered geopotential level, the location of the real eddy center N can be approximated. N$isthenthecenteroftheellipse.N$ is also taken as the center of the local $f-$plan Cartesian frame $(N, \vec{x}, \vec{y})$, where $\vec{x}$ is the zonal vector and $\vec{y}$ is the meridional vector. Starting from N, 1° north and 1° east are converted into horizontal and vertical length scales.
3. On this $f-$ plane, the line (NC) can be drawn, and depending on its orientation with respect to the parallels, we set it as the semi-major axis or the semi-major axis, following the results of G. Chen et al. (2019). Since they obtained a global distribution of semi-major axis orientations for best-fit vortex ellipses, we can determine which (NC) is more likely. Then P' and Q', two points on the ship's orbit, are computed such that $Q'C = CP'$.
4. In a 2D Cartesian frame, 5 points are needed to compute the exact equation of an ellipse. Here, our ellipse is initially constrained by its center N, the orientation of the semimajor (or semiminor) axis (NC), and the eccentricity imposed by the work of G. Chen et al. (2019). However, adding the two points P' and Q' will over-constrain the problem (considering its equations). Therefore, a choice must be made between P' and Q' to add a unique final constraint. As a consequence, two ellipses can be obtained: one passing through the point P', arbitrarily called (E_1), and one passing through the point Q', arbitrarily called (E_2). In the following steps, P' will be used arbitrarily to explain the procedure.
5. In polar coordinates, if (NC) is the orientation of the semi-major axis, the semi-major axis b can be obtained by

$$b = |NP|\sqrt{1 - \varepsilon^2 \cos^2 \theta_1} \tag{20}$$

   where $|NP| > 0$ is the Cartesian distance between N and P, ε is the imposed eccentricity, and $\theta_1 > 0$. If (NC) is the orientation of the semi-minor axis, we replace θ_1 with $\frac{\pi}{2} + \theta_1$. Then we can calculate the semi-major axis a:

$$a = \frac{b}{\sqrt{1 - \varepsilon^2}} \tag{21}$$

6. Finally, the ellipse equation reads

$$\left(\frac{x\cos\alpha + y\sin\alpha}{a}\right)^2 + \left(\frac{-x\sin\alpha + y\cos\alpha}{b}\right)^2 = 1 \tag{22}$$

   where α is defined in the figure 4, x and y are the two variables associated with the zonal and meridional axes respectively. The approximate volume is: $\Omega = \int_{-H}^{0} \pi a(z)b(z)dz$

for a surface vortex. For a subsurface vortex the boundary conditions have to be changed as in the previous part.

This method defines the uncertainty due to resolution as

$$\frac{\delta\Omega}{\Omega} = \frac{\int_{-H-\delta(dz)}^{0} \pi(a(z)+\delta(dx))(b(z)+\delta(dx))dz - \int_{-H}^{0} \pi a(z)b(z)dz}{\int_{-H}^{0} \pi a(z)b(z)dz} \tag{23}$$

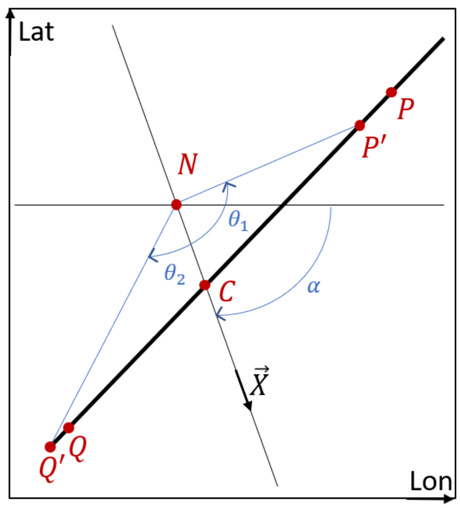

Figure 4. Main geometric constructions for solving ellipse equations.

This method preserves the non-axisymmetry of the eddy and takes into account the vertical structure. The center is that of the Nencioli et al. (2008) routine, which remains an approximation but gives a better estimate than the previous method. The elliptical shape is more common than the circular shape among vortices. Note, however, that this method requires that N and C be on the same semi-major (or minor) axis and that the eccentricity be known. Two ellipses can be determined by this method (there is no uniqueness). Furthermore, the real upper and lower limits of the core remain unknown, and our method extrapolates in this region. Indeed, in the ship section, the upper and lower limits are characterized by the fact that P and Q tend to C, so that PQ tends to vanish. However, looking at equation (13), the semi-major axis will not remain zero when approaching these boundaries. To avoid this side effect, ellipses are found only at the geopotential level where $PQ \neq 0$. Therefore, the volume will be underestimated.

5 Results

5.1 Heterogeneous waters in eddy cores

For each mesoscale eddy, thermohaline anomalies on the isopycnals have been computed using the methodology described in Section 3.1. Examples of anomalies computed for some eddies are shown in Figure 5. We inform the reader that all other vertical sections can be found in the supplementary materials, figures S1 to S16. Both salinity and temperature anomalies are calculated for each eddy.

For the subsurface AC sampled in the Lofoten Basin ($N°$ 26 in Table 2), a significant thermohaline anomaly is visible in the middle of the temperature and salinity panels between -700m and -1150m depth. The location of this anomaly coincides with the

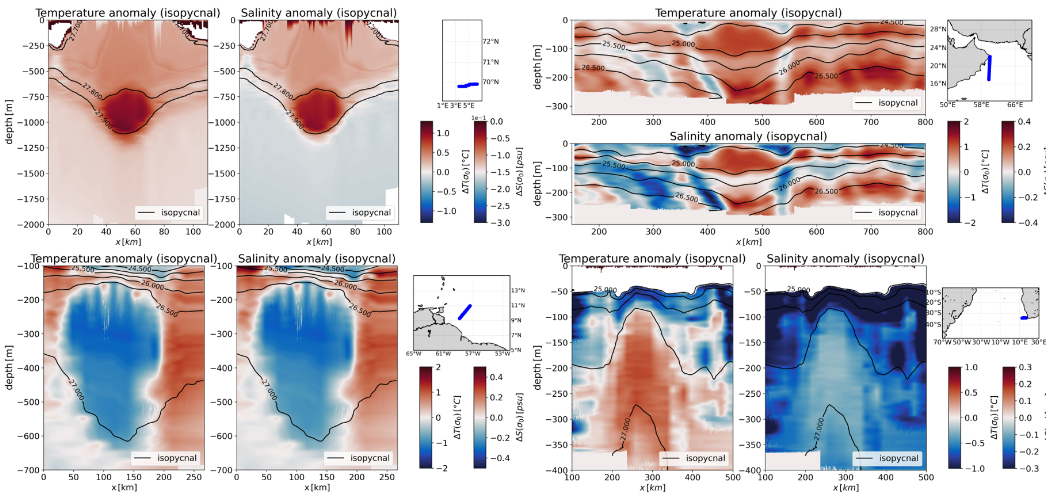

Figure 5. Thermohaline anomalies on isopycnals computed for mesoscale eddies: the Lofoten Basin anticyclone ($N°26$), the Persian Gulf anticyclone dipole ($N°7$), the North Brazil Current anticyclone ($N°2$), and the Southern Cape Basin cyclone ($N°9$). For each gyre, three panels are shown: both temperature and salinity anomalies, and a small map showing the transect (in blue) along which the eddy was sampled. For panels showing anomalies, the abscissa axis is the horizontal scale in km and the ordinate axis is the depth in m. Isopycnals are shown in black. The white bands near the bottom indicate where the data ends. The white regions near the surface illustrate the fact that in some cases the lowest potential density value of the climatological mean is higher than the lowest value of the vertical profiles, anomalies on isopycnals cannot be computed in these regions.

maximum isopycnal anomaly, indicating that it corresponds to the eddy core. The trapped water is warmer and fresher than the climatological average. Compared to the surrounding water, the trapped water appears warmer and saltier.

A distinct negative anomaly can be observed in the vertical sections of the subsurface AC sampled during EUREC4A-OA ($N°\ 2$). This eddy transports water that is fresher and colder than the surrounding water. In the case of the surface AC sampled during Physindien 2011, the warmer and saltier core is located at $x \approx 470$km and is surrounded by colder and less salty water that forms a rim around it. The subsurface cyclone sampled during M124 also shows anomalies in the region where the isopycnals show the greatest anomaly. Water that is hotter and saltier than its surroundings is trapped in the eddy core. However, the core is less well localized than in other examples, suggesting either that the eddy is losing water through instability and filamentation, or that it is not well resolved in terms of horizontal resolution of vertical thermohaline properties.

In Table 5 the maximum values of thermohaline anomalies on isopycnals are collected for each eddy. The anomalies are calculated with respect to climatological averages. An eddy is considered to be materially coherent when the maximum anomaly is reached at the eddy center (region where the velocity tends to zero) and there is a marked difference in values between the enclosed and surrounding waters.

According to the data, 22 out of 26 eddies have a significant thermohaline anomaly on isopycnals in their core. Thus, 84.6% of the eddies are found to transport heterogeneous water in their core. Even eddies sampled far from their origin showed an anomaly in their core (see Agulhas rings $N°15,\ 16,\ 17$)). Since the number of eddies studied is

Table 5. Maximum values for temperature and salinity anomalies on isopycnals (anomalies calculated with respect to the climatological mean). These values are reached in the eddy cores. If there is no clear maximum in an eddy core, the enclosed water is not different from the surrounding water; this is indicated by a dash: the eddy is then considered to be not materially coherent. The last column indicates its Material Coherence (MC). Note that the presence of the eddy center in a vertical section is not required to evaluate the MC.

Num	Cruise	Type	max(ΔT) [$°C$]	max(ΔS) [psu]	MC [yes/no]
1	EUREC4A-OA	AC	-0.86	-0.34	Yes
2	EUREC4A-OA	AC	-1.6	-0.64	Yes
3	EUREC4A-OA	AC	-0.65	-0.24	Yes
4	MSM60	C	0.87	0.18	Yes
5	MSM60	C	0.3	-0.05	Yes
6	MSM60	C	-	-	No
7	PHY11	AC	1.55	0.28	Yes
8	PHY11	AC	2.55	0.63	Yes
9	M124	C	0.53	-0.07	Yes
10	M124	AC	0.46	-0.05	Yes
11	M124	AC	0.52	-0.03	Yes
12	M124	AC	0.49	-0.04	Yes
13	M124	AC	0.49	-0.04	Yes
14	M124	AC	0.66	0.01	Yes
15	M124	AC	0.73	0.04	Yes
16	M124	AC	0.81	0.06	Yes
17	M124	AC	0.49	-0.04	Yes
18	MSM74	AC	0.67	-0.08	Yes
19	MSM74	C	-0.78	-0.27	Yes
20	MSM74	C	-1.09	-0.31	Yes
21	MSM74	C	-	-	No
22	MSM74	AC	-	-	No
23	m160	C	-	-	No
24	KB2017606	AC	1.34	-0.02	Yes
25	KB2017606	AC	1.12	-0.03	Yes
26	HM2016611	AC	1.09	-0.04	Yes

small compared to those derived from global satellite altimetry, only hypotheses can be formulated. One can wonder if material coherence is more common than studies based on satellite altimetry have indicated so far.

5.2 Location of heterogeneous water

In figure 6, sampled eddies are confronted with eddies detected by the TOEddies algorithm. Our confrontation will be qualitative, as we will only discuss the surface or subsurface character of eddies. We will leave the quantitative aspects to a future study. This figure focuses on 17 well-sampled eddies that provide important information. Only eddies $N°3$, 8 do not appear, because they are completely below the surface. We refer the reader to the supplementary material for more details on these eddies. The purpose here is to present cases where the use of satellite altimetry data could lead to some misinterpretations.

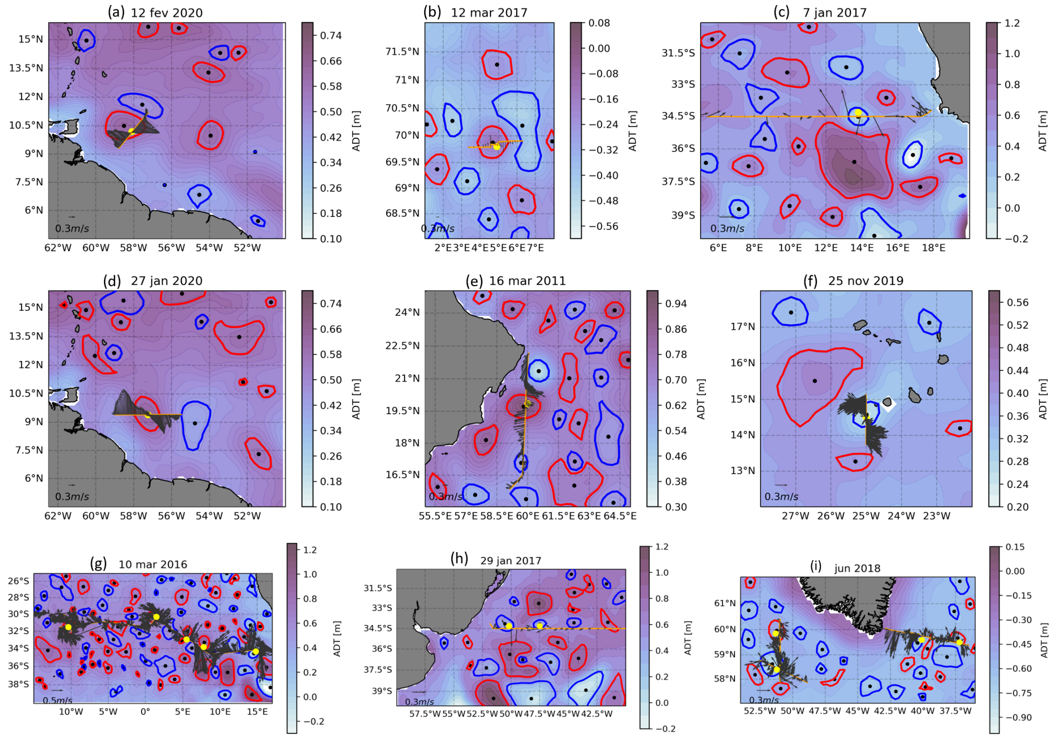

Figure 6. Comparison between satellite altimetry data and *in situ* data for some eddies. Each panel shows the same elements: ADT [m] as colored background, anticyclonic eddies (red contours) and cyclonic eddies (blue contours) detected by the TOEddies algorithm, eddy centers (dark dots) also detected by the TOEddies algorithm, the ship track in orange, velocity vectors at a given depth in gray (the legend is given for each panel), and the eddy centers estimated at this depth level using the Nencioli et al. (2008) routine in yellow dots. Panel (a): AC $N°2$ and velocity field at -300m depth. Panel (b): AC $N°25$ and velocity field at -900m depth. Panel (c): C $N°4$ and velocity field at -50m depth. Panel (d): AC $N°1$ and velocity field at -50m depth. Panel (e): AC $N°7$ and velocity field at -50m depth. Panel (f): C $N°23$ and velocity field at -50m depth. Panel (g): AC $N°10$, 11, 13, 17, C $N°9$ and velocity field at -100m depth. Panel (h): C $N°5$, 6 and velocity field at -50m depth. Panel (i): AC $N°18$, 22 and C $N°20$, 21 and velocity field at -50m depth.

Let us first look at panel (a). This panel is about the subsurface eddy $N°2$, which is also shown in figure 5. TOEddies detects this eddy as an anticyclone. The materially coherent core of the vortex (location of the anomaly) is below $-150m$ and the velocity field tends to zero at this geopotential level. Thus, while the TOEddies correctly detects an anticyclonic eddy, the eddy does not correspond to a surface intensified eddy. In fact, analogous cases have been discussed in Laxenaire et al. (2018); Subirade et al. (2023). Therefore, information on the vertical structure of the eddy is crucial for assessing the structure and nature of eddies from satellite altimetry data.

Panel (b) shows another example of an eddy, the eddy $N°25$, which is also shown in Fig. 5. Again, the ADT signature of the eddy corresponds to the actual sampled eddy. In this case, the ADCP velocity field is not zero at the surface. However, the materially coherent core is located at about -1000m depth and cannot be detected as such by satellite altimetry. This is also the case for panels (c), (d), (e), (f), (g), and (h). Some eddies have a velocity imprint at the sea surface, but the trapped heterogeneous water is much deeper. Again, the supplementary material shows thermohaline anomalies on isopycnals for each eddy discussed in this article.

In our data set, the maximum thermohaline anomaly is often at depth rather than at the surface, even for eddies detected by satellite altimetry. However, our study highlights the limitations of using satellite altimetry or any surface field alone to infer eddy properties. By considering only the geostrophic velocity fields derived from satellite altimetry or other surface properties, the derived eddy assessments miss the vertical properties of eddies. This is especially true for subsurface intensified eddies. Lagrangian studies suggest that the ability of eddies to trap a water mass is a consequence of closed trajectories. However, such trajectories cannot be computed from surface velocity fields alone. In fact, as we have seen here, many eddies are subsurface intensified. This is even more true when using geostrophic velocities derived from satellite altimetry data. In fact, most observed in-situ velocities differ from geostrophic velocities, even when a cyclostrophic component is included. Also, the horizontal resolution of satellite altimetry is relatively poor compared to the eddy dimensions and varying eddy velocity. Therefore, by integrating the geostrophic velocities derived from satellite altimetry, the Lagrangian estimates of water parcel trajectories provide a biased diagnostic of eddy material coherence. In fact, many eddies are defined as non-coherent while they are when the entire water column is analyzed.

Consequently, tracer transport estimates depend critically on how eddies are observed and characterized. Note the proportion of thermohaline subsurface intensified eddies, 60.7%, in our *in situ* dataset. Even if the number of surface intensified eddies is underestimated, because *in situ* measurements often sample the ocean below $-50m$ depth, this ratio emphasizes the ubiquity of subsurface eddies and the bias of studies based on altimetry alone that do not account for them.

In summary, in most cases velocity is correlated with thermohaline anomalies on isopycnals. However, there are a significant number of eddies detected by satellite altimetry that are subsurface enhanced and characterized by a deep maximum of velocity and thermohaline anomalies. These eddies increase the uncertainty of tracer transport estimates based on satellite altimetry data alone.

5.3 Volume estimates

5.3.1 3D Eddy Boundary Characterisation

For materially coherent eddies, our ultimate goal is to calculate their volume to quantify their contribution to tracer transport. As mentioned in the methodology section, it is difficult to calculate the eddy volume with a single ship section; moreover, this calculation depends on the criteria used to delimit the core.

In this section, the eddy volume calculated in this way is analyzed along with 6 eddy core boundary criteria: Thermohaline anomalies on isopycnal surfaces (see equations (1) and (2)), relative vorticity (equation (5)), Brunt Vaisala frequency (equation (4)), norm of the 2D buoyancy gradient (equation (3)), EPV anomaly (equation (9)), and the ratio $\frac{\Delta EPV_z}{EPV_x}$ (equation (10)). Depending on the data resolution and noise, some criteria may not be applicable.

Here three well-sampled AC ($N^{\circ}1,\ 7$ & 25, denoted C^{+} in table 3) have been selected for which the 6 criteria can be applied. Eddy $N^{\circ}1$ (the surface AC sampled during EUREC4A-OA) and eddy $N^{\circ}7$ (the surface AC sampled during Physindien 2011) have the finest horizontal resolution, so the uncertainties are small. Eddy $N^{\circ}26$ (the subsurface AC sampled in the Lofoten Basin) has a sharp boundary; although its sampling is not optimal, its structure raises interesting questions.

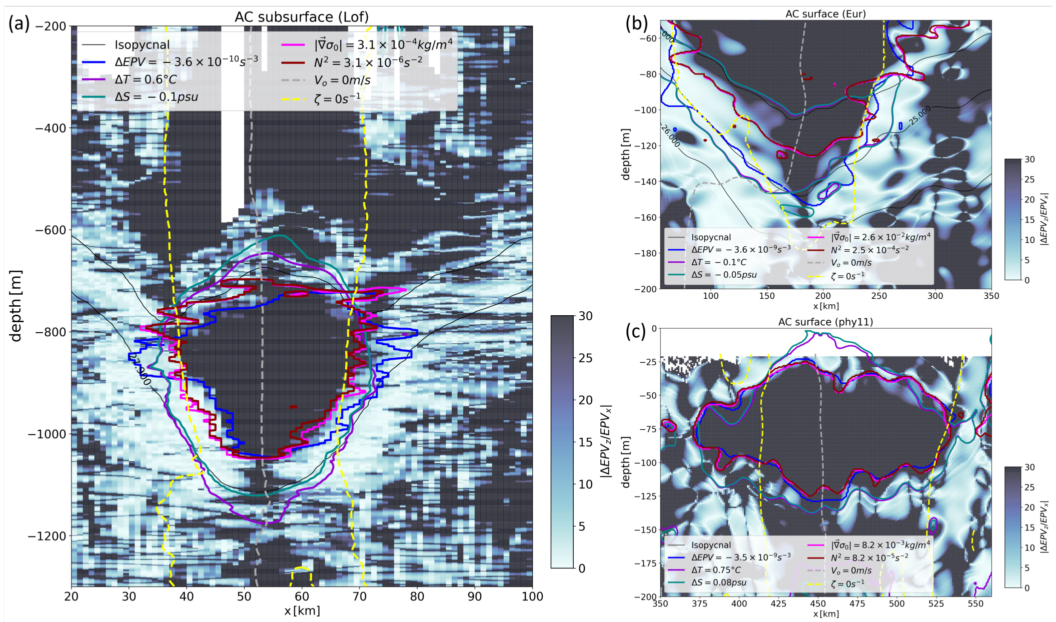

Figure 7. Outermost closed eddy contours computed using 5 criteria: thermal anomalies on isopycnal surfaces in purple, salinity anomalies on isopycnal surfaces in green, relative vorticity in dashed yellow, Brunt-Väisälä frequency in brown, density gradient norm in pink, EPV anomaly in blue. The $\frac{\Delta EPV_z}{EPV_x} > 30$ criterion in the background is also able to capture the stable core of eddies 1 (panel (b)), 7 (panel (c)), and 25 (panel (a)). The color associated with this quantity has been saturated at level 30 to capture the region of weak frontality. The apparent eddy center is shown as a dashed gray line, the isopycnals as thin dark lines. The eddy center divides the core into two parts: the left (or right) side is used to determine the volumes using the ellipses (E_1) (or (E_2)). The horizontal smoothing periods for panels (b) and (c) have been increased to 30km so that the boundaries appear clearly.

The methods presented are carefully followed. Figure 7 shows the vertical section of the ship overlaid with closed contours defined by the criteria for the 3 eddies considered. For the sake of clarity, the quantities used to draw the contours are calculated only in the vicinity of the core. In reality, due to the noise in the data, these criteria can also detect other features not related to the eddy core. In the background, the quantity $\frac{\Delta EPV_z}{EPV_x}$ is plotted. The eddy volume is insensitive to the threshold chosen for $\frac{\Delta EPV_z}{EPV_x}$ because its gradient is very pronounced at the eddy boundary. The difference in the eddy volume when choosing levels 10 or 30 is less than 3%. However, this threshold must be greater than 10 for EPV_x to be negligible before ΔEPV_z.

As an example, in panel (a) this criterion highlights the deep core of the eddy between -650m and -1050m. Above this core, for $\sigma_0 \in [27.7; 27.8] kg/m^3$, the quantity $\frac{\Delta EPV_z}{EPV_x}$ decreases slightly: this marks the upper boundary of the core. Below this core, where $\sigma_0 > 27.88 kg/m^3$, the quantity $\frac{\Delta EPV_z}{EPV_x}$ decreases rapidly to values below 5, forming the lower vortex boundary. The lateral eddy boundary is characterized by $EPV_x \approx \Delta EPV_z$, indicating that it is subject to symmetric instability.

This key finding is supported by the other five criteria. The region where $\frac{\Delta EPV_z}{EPV_x} > 30$ is consistent with the region where: thermohaline anomalies on isopycnals reach an extremum; the core is quite homogeneous according to the density gradients and is associated with a significant anomaly of potential vorticity. However, the relative vorticity seems to be less relevant for the detection of the upper and lower core boundaries. Since this criterion only considers the velocity field, it does not distinguish materially coherent regions from others. As a result, the approximated volume appears much larger than that determined by the other criteria.

It is worth noting that the region where $\sigma_0 < 27.7kg/m^3$ is also characterized by the $\frac{\Delta EPV_z}{EPV_x} > 30$ criterion, although the materially coherent core appears to lie below it. In fact, since EPV lies on buoyancy gradients, a non-materially coherent region can be highlighted by buoyancy gradients created by isopycnal deviations. This shallower region is also consistent with the region where $\zeta_z < 0$.

Similar observations can be made for panels (b) and (c). As mentioned in section 3.4, the criterion based on $\frac{\Delta EPV_z}{EPV_x}$ is only efficient in regions where heterogeneous water is trapped.

5.3.2 3D eddy reconstruction

In this section, methods for approximating eddy volumes are applied to the three eddies considered, but results are shown only for the AC of panel (a) in Figure 7. The eddy shapes are discussed before the numerical aspects are presented.

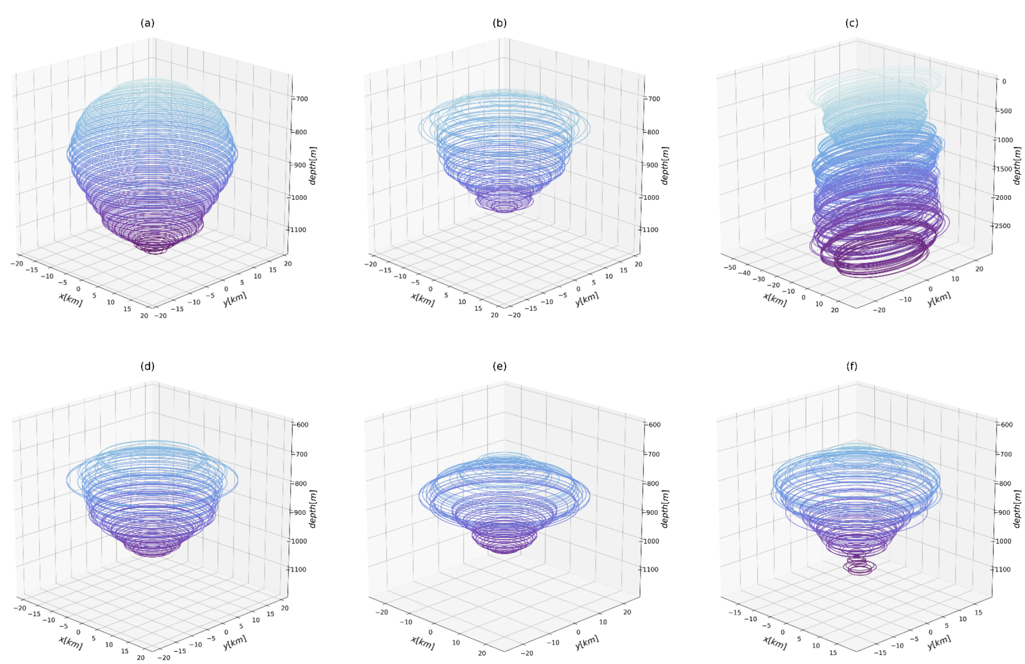

Figure 8. 3D reconstructions of AC $N°26$ assuming its circularity at each geopotential level. Each panel corresponds to one criterion. The criteria are detailed in figure 7. (a): Thermal anomaly on isopycnals, (b): Brunt-Väisälä frequency, (c): relative vorticity, (d): norm of 2D density gradient, (e): Ertel potential vorticity anomaly, (f): $\frac{\Delta EPV_z}{EPV_x}$. Contours are plotted every five meters.

Figure 8 shows the 3D reconstructions assuming circularity of the eddy at each geopotential level. Since the position of the center does not vary with depth, the eddy is axisymmetric. The reconstructed volume associated with the thermal anomaly is the most convex of all shapes. The eddy shape using the relative vorticity criterion is almost cylindrical and its upper and lower boundaries cannot be clearly distinguished. On the contrary, any other criterion leads to an eddy radius that decreases near the upper and lower boundaries: the volume is closed. Using the criterion on the norm of the 2D density gradient gives a similar shape to the Brunt-Väisälä frequency criterion. Except for the relative vorticity criterion, the eddy core is top shaped. The criterion on $\frac{\Delta EPV_z}{EPV_x}$ leads to a more conical eddy than the criteria based on gradients.

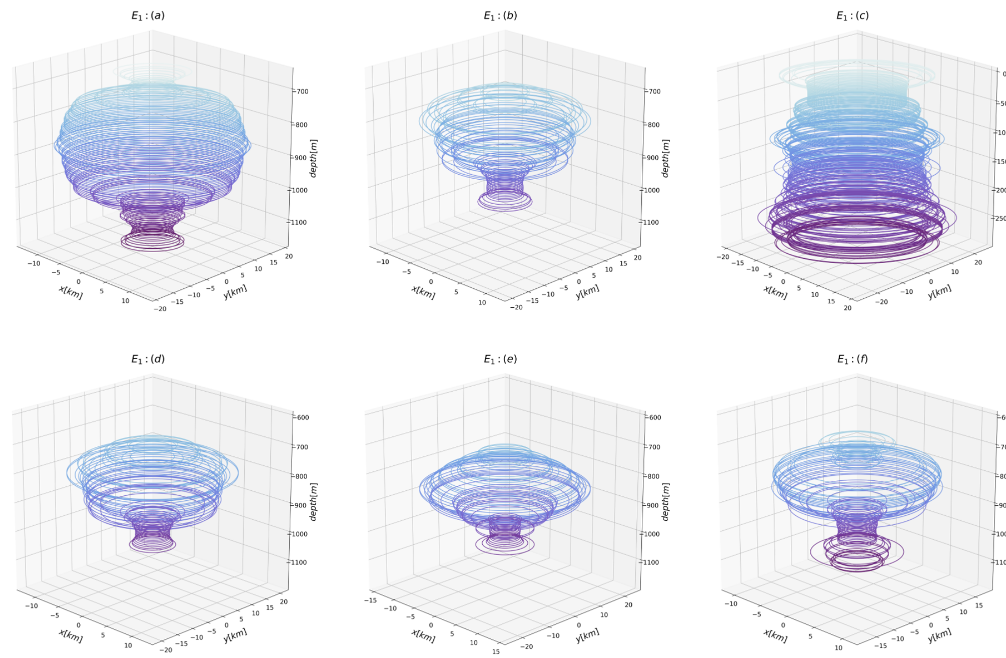

Figure 9. 3D reconstructions of AC $N°26$ assuming the ellipticity of the eddy at each geopotential level. Each panel corresponds to a criterion. The criteria are detailed in figure 7. (a): Thermal anomaly on isopycnals, (b): Brunt-Väisälä frequency, (c): Relative vorticity, (d): 2D density gradient norm, (e): Ertel potential vorticity anomaly, (f): $\frac{\Delta EPV_z}{EPV_x}$. Contours are plotted every five meters.

Figure 9 shows the 3D reconstructions assuming the vortex core is elliptical at each geopotential level. For $N°1$ the eccentricity is set to 0.782, for $N°7$ the value of 0.780 is kept, and for $N°26$ the value of 0.792 is kept. This figure refers to the ellipses ($E1$) mentioned earlier: the left side of the core was used to construct the volume. Again, the relative vorticity criterion leads to a cylindrical vortex shape. For all other criteria, the eddy base is thinner than for circular eddies (see figure 8). This is consistent with figure 7, where the eddy bottom radius is smaller on the left than on the right. As before, criteria based on the Brunt-Väisälä frequency or on the norm of the 2D density gradient give eddy shapes similar to those with the $\frac{\Delta EPV_z}{EPV_x}$ criterion.

Figure 10 shows the 3D reconstructions again assuming the ellipticity of the eddy core at each geopotential level, this time using the right side of the core (ellipses E_2) to construct volumes. In this case, the shapes are quite similar to those in figure 8, but the eddy volumes are larger. The thermal anomaly criterion results in a very convex shape.

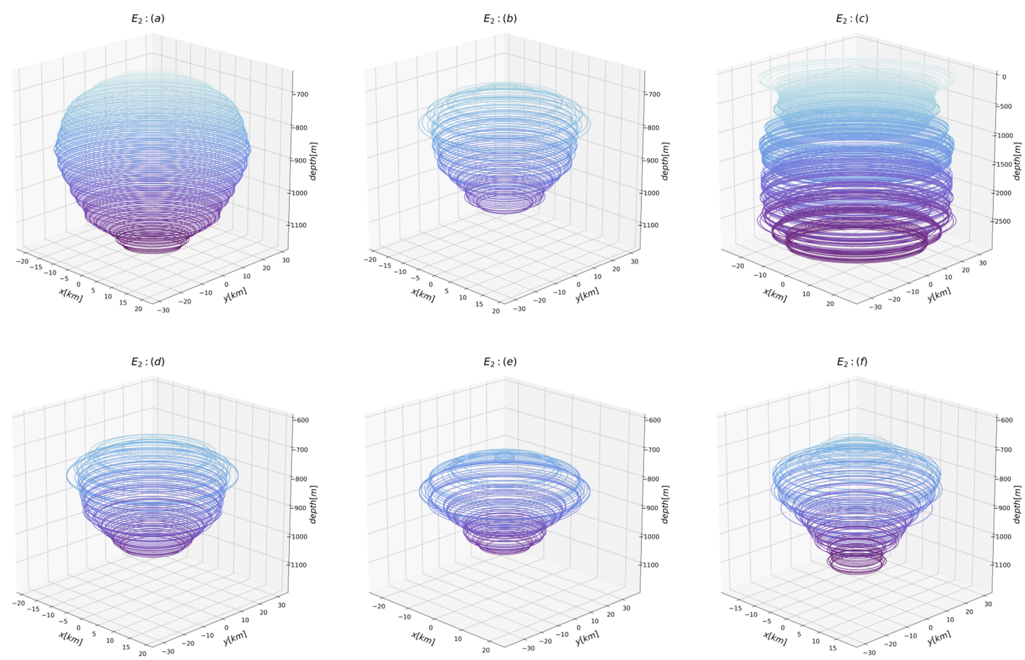

Figure 10. 3D reconstructions of AC $N°26$ assuming its ellipticity at each geopotential level. Each panel corresponds to a criterion. The criteria are detailed in figure 7. (a): Thermal anomaly on isopycnals, (b): Brunt-Väisälä frequency, (c): Relative vorticity, (d): 2D density gradient norm, (e): Ertel potential vorticity anomaly, (f): $\frac{\Delta EPV_z}{EPV_x}$. Contours are plotted every five meters.

The Brunt-Väisälä frequency criterion and the 2D density gradient norm give shapes similar to those of the circular eddy. Except for the relative vorticity criterion, the bottom of each eddy is thinner than the top, similar to figure 8. We also recover the conical eddy using the criterion on $\frac{\Delta EPV_z}{EPV_x}$.

5.3.3 Eddy Volume Comparison

The volumes and uncertainties for the three eddies considered are now calculated and summarized in Figure 11. For each eddy, the volume has been normalized to the cylindrical volume $\Omega_0 = \pi L^2 H$, where L and H are given in Table 3 (note that L is defined in Figure 1). The normalized volumes for circular vortices are obviously closer to 1 than for ellipses.

For any approximation method (circular or elliptical), the volume depends on the chosen criterion. For example, assuming the circularity of the eddy $N°26$, the volume is twice as small with the $\frac{\Delta EPV_z}{EPV_x}$ criterion as with the thermal anomaly criterion. Conversely, for a given criterion, the method based on ellipses gives larger volumes than the circular approximation. As expected, the relative vorticity criterion overestimates the entrapped volume. The criteria based on the Brunt-Väisälä frequency, the norm of the 2D density gradient, the EPV anomaly, and $\frac{\Delta EPV_z}{EPV_x}$ give closer values regardless of the method used.

In all cases, the approximation of the volume by a cylinder of constant radius (Ω_0 in figure 11) with *in situ* data leads to an overestimation of the trapped volume compared to the reconstruction using circles (”circ” in figure 11). Conversely, for elliptical shapes, the tracer transport seems to be overestimated compared to the constant radius approximation.

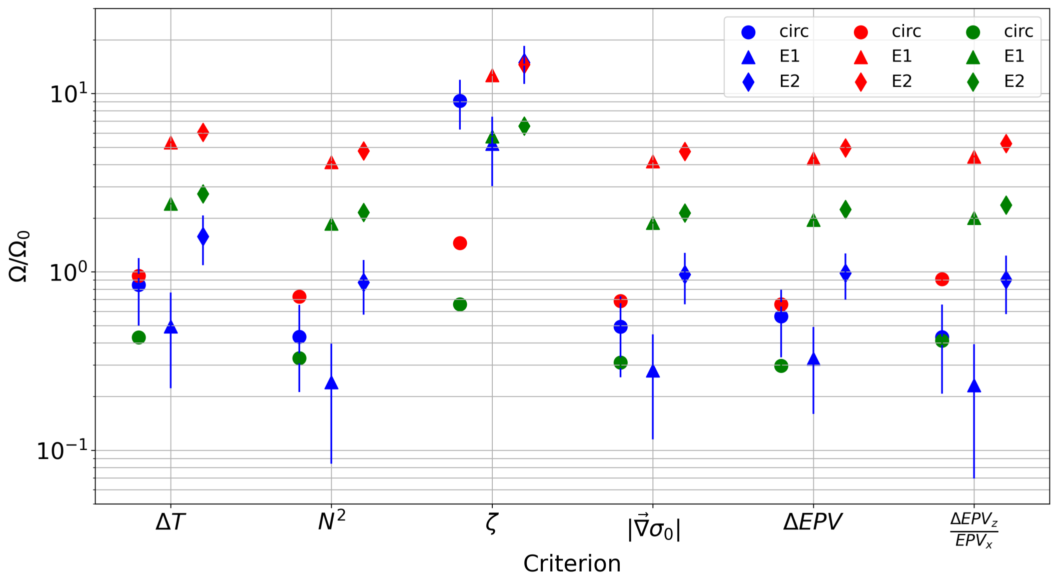

Figure 11. Normalized volume as a function of criterion used, for eddies $N°1$ (green markers), $N°7$ (red markers), $N°26$ (blue markers) using the two reconstruction methods. Normalized volumes are plotted by criterion and by method. Error bars have been added, but are only visible for AC $N°26$ because the horizontal resolution of AC $N°1$ and $N°7$ is finer than 3% of the apparent eddy radius L. Since the volumes obtained with the relative vorticity criterion are much larger than those obtained with the other criteria, a logarithmic scale has been used.

Using the $\frac{\Delta EPV_z}{EPV_x}$ criterion as a reference, relative differences with other criteria have been calculated and are shown in Figure 12. As mentioned above, thermohaline anomalies on isopycnals lead to a larger volume estimate than with the $\frac{\Delta EPV_z}{EPV_x}$ criterion (see Figure 7) and the relative difference between the volumes is large. For example, AC $N°26$ has twice the volume with thermohaline anomalies than with the $\frac{\Delta EPV_z}{EPV_x}$ criterion. The relative error between EPV anomaly and $\frac{\Delta EPV_z}{EPV_x}$ is also noticeable, reaching more than 30% for eddy $N°1$. Since the EPV anomaly is calculated using the horizontal contribution EPV_x, and since this term increases near the boundary, the total volume increases even as EPV_z decreases. Physically, the region where EPV_x is large is more likely to experience frontal instabilities. Therefore, the water properties in this region can change due to mixing and the core can decay. As a consequence, the materially coherent core is somewhat overestimated by ΔEPV.

Finally, the most remarkable result is that the volume obtained with the N^2 criterion is a good approximation of that obtained with $\frac{\Delta EPV_z}{EPV_x}$. In fact, the relative error between the two computed volumes does not exceed 20%, regardless of the eddy and the method used. The criterion-based norm of the 2D density gradient also gives similar results to the latter two, which is consistent with their mathematical definitions. In fact, eddies modify the local stratification due to their trapped water; this creates a baroclinic contribution to the buoyancy field. Consequently, the calculation of N^2 reflects the eddy core. To illustrate this last point, Meunier et al. (2021) performed a decomposition of EPV into three terms for an eddy sampled by gliders in the Gulf of Mexico; they showed that eddy stretching (related to the vertical buoyancy gradient) was the dominant term.

Our conclusions from Figure 12 are consistent with this result and our theoretical development in Section 3.4.

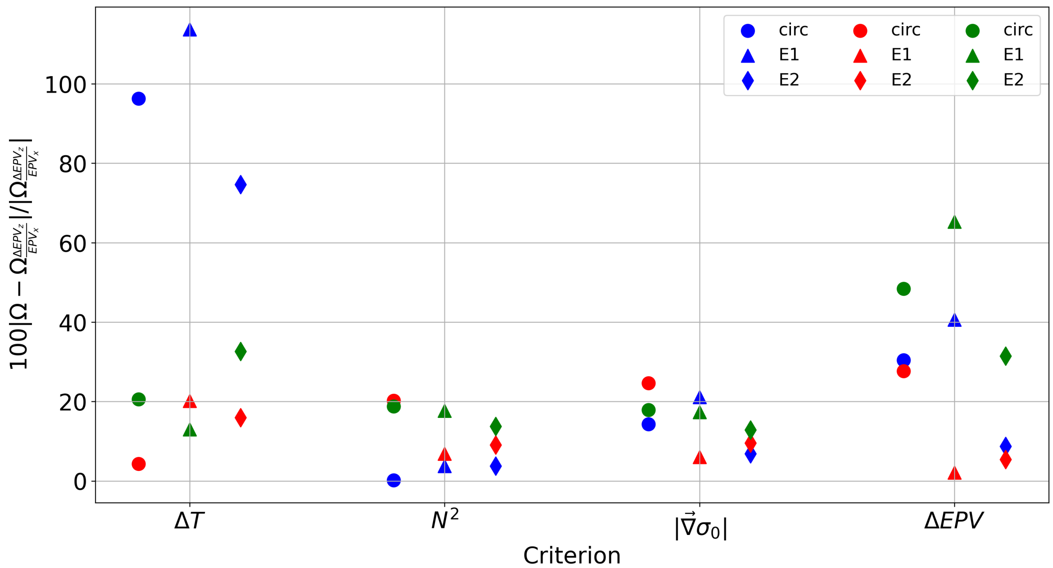

Figure 12. Relative gap between volume approximations using that of $\frac{\Delta EPV_z}{EPV_x}$ as a reference. As in figure 11, results are plotted for eddies $N°1$ (green markers), $N°7$ (red markers), $N°26$ (blue markers)

6 Conclusion

In this paper we have evaluated the transported volume of mesoscale eddies using in situ data collected during several cruises (mostly in the Atlantic Ocean).

By analyzing the relative errors, we have shown that the horizontal resolution of the hydrographic data (CTD, uCTD) and the vertical resolution of the velocity data are the most critical parameters for calculating the gradients of the physical quantities. Relative errors can reach 50% in the worst cases. Considering the size of mesoscale eddies, future cruises should perform hydrographic measurements with a horizontal resolution finer than 10% of the eddy radius (which gives 5km for and eddy of radius 50km) and velocity measurements with vertical bins smaller than 5% of the eddy vertical extension (which gives 15m for a vertical extent of 300m). It is also worth noting that very few cruises sampled eddy boundaries accurately and completely. This is an important feature to focus on in future cruises.

Despite the moderate resolution of our data and the small number of eddies considered, we have shown that materially coherent eddies are not exceptional. However, materially coherent eddy cores are often located below the pycnocline and therefore cannot be detected as such using analyses based solely on satellite altimetry data. In fact, subsurface eddies are either undetectable on such fields, or if they are, the derived surface geostrophic velocity is not the appropriate velocity field to infer the material coherence of the eddy. We advise future studies to be careful when using the terms ”surface” or ”subsurface”, as eddies can trap their water mass much deeper than the pynocline.

For materially coherent eddies, a criterion developed by Barabinot et al. (2024) based on EPV characterizes the eddy boundary, but indicates that it is subject to instabilities on small scales. Therefore, some of the water trapped by eddies and characterized by thermohaline anomalies may escape from these eddies. Moreover, not only can fluid particles escape from the core, but they can also undergo some thermohaline changes at the eddy boundary due to turbulent diffusion. Future studies should investigate and quantify the permeability of the eddy boundary to calculate the heat and salt volume lost during a time unit. This is not an easy task as it involves meso and submeso scale processes.

We then proposed two methods to extrapolate the eddy volume using a single ship section. The first method assumes circularity of the eddy at each geopotential level and yields lower volumes than the second method, which assumes ellipticity of the eddy core. Volumes were also calculated and compared for different criteria. The outermost closed contour of the Brunt-Vaisala frequency is a good approximation for the materially coherent eddy core. This result confirms the conclusions of previous studies. This conclusion is also relevant for the study of eddies using ARGO profiler data.

Obviously, future studies are needed to confront thermohaline anomalies and Lagrangian criteria, and thus to assess the material coherence in depth by temporal monitoring. We are reaching the limits of available *in situ* data for this purpose.

Acknowledgments

This research was supported by the European Union's Horizon2020 research and innovation program under grant agreement no. 817578 (TRIATLAS), the Centre National d'Etudes Spatiales through the TOEddies and EUREC4A-OA projects, the French National Program LEFE INSU, IFREMER, the French Vessel Research Fleet, the French Research Infrastructures AERIS and ODATIS, IPSL, the Chaire Chanel Program of the ENS Geosciences Department, and the EUREC4A-OA JPI Ocean and Climate Program. we thank all the people who collected, processed and made public the data as well as all the institutions for which these people worked in particular the University of Bergen and GEOMAR Helmoltz Centre for Ocean Research Kiel. We also warmly thank every captain and crew of the RVs Atalante, Maria S. Merian, FS Meteor, RV Kristine Bonnevie and RV Hakon Mosby without whom this study could not have been carried out. Yan Barabinot is supported by a Ph.D. grant from the Ecole Normale Supérieure de Saclay. Xavier Carton acknowledges support from UBO and a CNES contract EUREC4A-OA.

Declaration of interests. The authors report no conflict of interest.

Data Availability Statement

In this study, we benefited from numerous data sets freely available and listed here.

The ADT produced by Ssalto/Duacs distributed by CMEMS, accessed on 19 January 2021:

https://resources.marine.copernicus.eu

The concatenated RVs Atalante and Maria S Merian hydrographic and velocity data (L'Hegaret Pierre, 2020) are freely available on the SEANOE website :

https://www.seanoe.org/data/00809/92071/, accessed on 15 March 2021.

The hydrographic and velocity measurements taken during the M124 cruise (Karstensen & Wölfl, 2016; Karstensen et al., 2016; Karstensen & Krahmann, 2016) of the RV Meteor are freely available on the PANGAEA web site:

https://doi.org/10.1594/PANGAEA.902947, https://doi.pangaea.de/10.1594/PANGAEA.863015, https://doi.pangaea.de/10.1594/PANGAEA.869740.

The hydrographic and velocity data collected during the M160 cruise (Dengler, Fischer, et al., 2022; Dengler, Körtzinger, & Krahmann, 2022a, 2022b) of the RV Meteor are freely available on the PANGAEA web site:

https://doi.org/10.1594/PANGAEA.943409, https://doi.org/10.1594/PANGAEA.943432, https://doi.org/10.1594/PANGAEA.943657.

The hydrographic and velocity data collected during the MSM60 cruise (Karstensen, 2020b, 2020a) of the RV Meteor are freely available on the PANGAEA web site:

https://doi.pangaea.de/10.1594/PANGAEA.915879, https://doi.pangaea.de/10.1594/PANGAEA.915898

The hydrographic and velocity data collected during the MSM74 cruise (Karstensen & Krahmann, 2021; Karstensen & Czeschel, 2021) of the RV Meteor are freely available on the PANGAEA web site:

https://doi.pangaea.de/10.1594/PANGAEA.929000, https://doi.pangaea.de/10.1594/PANGAEA.928976

The hydrographic and velocity measurements along Physindien 2011 (L'Hégaret et al., 2016) are freely available on Ifremer website:

https://co-en.ifremer.fr/eulerianPlatform?contextId=8890&ptfCode=1901185&lang=en.

Finally, hydrographic and velocity data collected during the RV Kristine Bonnevie and RV Hakon Mosby KB2017606, HM2016611, KB2017618 cruise (Fer et al., 2019; Bosse et al., 2019) are freely available on the NMDC website:

https://doi.org/10.21335/NMDC-1093031037.

References

Barabinot, Y., Speich, S., & Carton, X. (2024). Defining mesoscale eddies boundaries from in-situ data and a theoretical framework. *Journal of Geophysical Research: Oceans*, *129*(2), e2023JC020422.

Bars, M. L., Aubert, O., Gal, P. L., & Marcus, P. S. (2011). Forme et persistance de tourbillons lenticulaires dans les écoulements stratifiés tournants : du laboratoire à la tâche rouge de jupiter !.

Beron-Vera, F. J., Wang, Y., Olascoaga, M. J., Goñi, G., & Haller, G. (2013). Objective detection of oceanic eddies and the agulhas leakage. *Journal of Physical Oceanography*, *43*, 1426-1438.

Bosse, A., Fer, I., Lilly, J. M., & Søiland, H. (2019). Dynamical controls on the longevity of a non-linear vortex : The case of the lofoten basin eddy. *Scientific Reports*, *9*. Retrieved from `https://api.semanticscholar.org/CorpusID:202580306`

Bretherton, F. P. (1966). Critical layer instability in baroclinic flows. *Quarterly Journal of the Royal Meteorological Society*, *92*, 325-334.

Carton, X. (2001). Hydrodynamical modeling of oceanic vortices. *Surveys in Geophysics*, *22*, 179-263.

Carton, X., Flierl, G. R., Perrot, X., Meunier, T., & Sokolovskiy, M. A. (2010). Explosive instability of geostrophic vortices. part 1: baroclinic instability. *Theoretical and Computational Fluid Dynamics*, *24*, 125-130.

Carton, X., & McWilliams, J. C. (1989). Barotropic and baroclinic instabilities of axisymmetric vortices in a quasigeostrophic model. *Elsevier oceanography series*, *50*, 225-244.

Chaigneau, A., Eldin, G., & Dewitte, B. (2009). Eddy activity in the four major upwelling systems from satellite altimetry (1992-2007). *Progress in Oceanography*, *83*, 117-123.

Charney, J. G. (1971). Geostrophic turbulence. *Journal of the Atmospheric Sci-*

ences, *28*(6), 1087–1095.
Chelton, D., Schlax, M. G., & Samelson, R. M. (2011). Global observations of nonlinear mesoscale eddies. *Progress in Oceanography*, *91*, 167-216.
Chen, G., Han, G., & Yang, X. (2019). On the intrinsic shape of oceanic eddies derived from satellite altimetry. *Remote Sensing of Environment*.
Chen, Y., Speich, S., & Laxenaire, R. (2022). Formation and transport of the south atlantic subtropical mode water in eddy-permitting observations. *Journal of Geophysical Research: Oceans*, *127*(1), e2021JC017767.
Chong, M. S., Perry, A. E., & Cantwell, B. J. (1990). A general classification of three-dimensional flow fields. *Physics of Fluids*, *2*, 765-777.
Crow, S. C., & Champagne, F. (1971). Orderly structure in jet turbulence. *Journal of fluid mechanics*, *48*(3), 547–591.
Cushman-Roisin, B. (1994). Introduction to geophysical fluid dynamics.
de Marez, C., Meunier, T., Morvan, M., L'Hégaret, P., & Carton, X. (2020). Study of the stability of a large realistic cyclonic eddy. *Ocean Modelling*.
Dengler, M., Fischer, T., Körtzinger, A., & Krahmann, G. (2022). *ADCP current measurements (38 and 75 kHz) during METEOR cruise M160* [data set]. PANGAEA. Retrieved from `https://doi.org/10.1594/PANGAEA.943409` doi: 10.1594/PANGAEA.943409
Dengler, M., Körtzinger, A., & Krahmann, G. (2022a). *Physical oceanography (CTD) during METEOR cruise M160* [data set]. PANGAEA. Retrieved from `https://doi.org/10.1594/PANGAEA.943432` doi: 10.1594/PANGAEA.943432
Dengler, M., Körtzinger, A., & Krahmann, G. (2022b). *Underway CTD data collected during METEOR cruise M160* [data set]. PANGAEA. Retrieved from `https://doi.org/10.1594/PANGAEA.943657` doi: 10.1594/PANGAEA.943657
Dong, C., & McWilliams, J. C. (2007). A numerical study of island wakes in the southern california bight. *Continental Shelf Research*, *27*, 1233-1248.
Dong, C., McWilliams, J. C., Liu, Y., & Chen, D. (2014). Global heat and salt transports by eddy movement. *Nature Communications*, *5*.
D'asaro, E., Lee, C., Rainville, L., Harcourt, R., & Thomas, L. (2011). Enhanced turbulence and energy dissipation at ocean fronts. *science*, *332*(6027), 318–322.
Eliassen, A. (1951). Slow thermally or frictionally controlled meridional circulation in a circular vortex. *Astrophisica Norvegica, v. 5, p. 19*, *5*, 19.
Ertel, H. (1942). Ein neuer hydrodynamischer erhaltungssatz. *Naturwissenschaften*, *30*, 543-544.
Fer, I., Bosse, A., Søiland, H., Ferron, B., & Bouruet-Aubertot, P. (2019). *Ocean currents, hydrography and microstructure data from provolo cruises* [data set]. NMDC. doi: https://doi.org/10.21335/NMDC-1093031037
Fjörtoft, R. (1950). Application of integral theorems in deriving criteria of stability for laminar flow and for the baroclinic circular vortex. *Geofysiske Publicationer*, *17*, 1-52.
Flierl, G. R. (1981). Particle motions in large-amplitude wave fields. *Geophysical and Astrophysical Fluid Dynamics*, *18*, 39-74.
Gent, P. R., & McWilliams, J. C. (1986). The instability of barotropic circular vortices. *Geophysical and Astrophysical Fluid Dynamics*, *35*, 209-233.
Goldsworth, F. W., Marshall, D. P., & Johnson, H. L. (2021). Symmetric instability in cross-equatorial western boundary currents. *Journal of Physical Oceanography*, *51*(6), 2049–2067.
Hadjighasem, A., Farazmand, M., Blazevski, D., Froyland, G., & Haller, G. (2017). A critical comparison of lagrangian methods for coherent structure detection. *Chaos*, *27 5*, 053104.
Haine, T. W., & Marshall, J. (1998). Gravitational, symmetric, and baroclinic insta-

bility of the ocean mixed layer. *Journal of physical oceanography*, *28*(4), 634–658.
Halle, C., & Pinkel, R. (2003). Internal wave variability in the beaufort sea during the winter of 1993/1994. *Journal of Geophysical Research*, *108*, 3210.
Haller, G. (2000). Finding finite-time invariant manifolds in two-dimensional velocity fields. *Chaos*, *10 1*, 99-108.
Haller, G. (2005). An objective definition of a vortex. *Journal of Fluid Mechanics*, *525*, 1 - 26.
Haller, G. (2015). Lagrangian coherent structures. *Annual Review of Fluid Mechanics*, *47*, 137-162.
Haller, G., Hadjighasem, A., Farazmand, M., & Huhn, F. (2015). Defining coherent vortices objectively from the vorticity. *Journal of Fluid Mechanics*, *795*, 136 - 173.
Herring, J. R. (1980). Statistical theory of quasi-geostrophic turbulence. *Journal of Atmospheric Sciences*, *37*(5), 969–977.
Hoskins, B. J. (1974). The role of potential vorticity in symmetric stability and instability. *Quarterly Journal of the Royal Meteorological Society*, *100*, 480-482.
Hoskins, B. J., & Bretherton, F. P. (1972). Atmospheric frontogenesis models: Mathematical formulation and solution. *Journal of the Atmospheric Sciences*, *29*, 11–37.
Hua, B. L., & Haidvogel, D. B. (1986). Numerical simulations of the vertical structure of quasi-geostrophic turbulence. *Journal of Atmospheric Sciences*, *43*(23), 2923–2936.
Hunt, J. C., Wray, A. A., & Moin, P. (1988). Eddies, streams, and convergence zones in turbulent flows. *Studying turbulence using numerical simulation databases, 2. Proceedings of the 1988 summer program*.
Hussain, A., & Zaman, K. (1980). Vortex pairing in a circular jet under controlled excitation. part 2. coherent structure dynamics. *Journal of fluid mechanics*, *101*(3), 493–544.
Hussain, A. F. (1986). Coherent structures and turbulence. *Journal of Fluid Mechanics*, *173*, 303–356.
Ioannou, A., Speich, S., & Laxenaire, R. (2022). Characterizing mesoscale eddies of eastern upwelling origins in the atlantic ocean and their role in offshore transport. *Frontiers in Marine Science*, *9*, 835260.
Ioannou, A., Stegner, A., Tuel, A., LeVu, B., Dumas, F., & Speich, S. (2019). Cyclostrophic corrections of aviso/duacs surface velocities and its application to mesoscale eddies in the mediterranean sea. *Journal of Geophysical Research: Oceans*, *124*(12), 8913–8932.
Joyce, T. M. (1977). A note on the lateral mixing of water masses. *Journal of Physical Oceanography*, *7*, 626-629.
Joyce, T. M. (1984). Velocity and hydrographic structure of a gulf stream warm-core ring. *Journal of Physical Oceanography*, *14*, 936-947.
Karstensen, J. (2020a). *Lowered ADCP data during MARIA S. MERIAN cruise MSM60/1* [data set]. PANGAEA. Retrieved from `https://doi.org/10.1594/PANGAEA.915879` doi: 10.1594/PANGAEA.915879
Karstensen, J. (2020b). *Physical oceanography (CTD) during Maria S. Merian cruise MSM60/1* [data set]. PANGAEA. Retrieved from `https://doi.org/10.1594/PANGAEA.915898` doi: 10.1594/PANGAEA.915898
Karstensen, J., & Czeschel, R. (2021). *ADCP current measurements (38 and 75 kHz) during Maria S. Merian cruise MSM74* [data set]. PANGAEA. Retrieved from `https://doi.org/10.1594/PANGAEA.929000` doi: 10.1594/PANGAEA.929000
Karstensen, J., & Krahmann, G. (2016). *Physical oceanography during METEOR cruise M124* [data set]. PANGAEA. Retrieved from `https://doi.org/10.1594/PANGAEA.863015` doi: 10.1594/PANGAEA.863015

Karstensen, J., & Krahmann, G. (2021). *Physical oceanography (CTD) during Maria S. Merian cruise MSM74* [data set]. PANGAEA. Retrieved from https://doi.org/10.1594/PANGAEA.928976 doi: 10.1594/PANGAEA.928976

Karstensen, J., Speich, S., Morard, R., Bumke, K., Clarke, J., Giorgetta, M., ... others (2016). Oceanic & atmospheric variability in the south atlantic cruise no. m124 29. february–18. march 2016 cape town (republic south africa)–rio de janeiro (brazil).

Karstensen, J., & Wölfl, A.-C. (2016). *Raw multibeam EM122 data: METEOR cruise M124 (SE Atlantic)* [data set]. PANGAEA. Retrieved from https://doi.org/10.1594/PANGAEA.869740 doi: 10.1594/PANGAEA.869740

Kline, S. J., Reynolds, W. C., Schraub, F., & Runstadler, P. (1967). The structure of turbulent boundary layers. *Journal of Fluid Mechanics*, *30*(4), 741–773.

Laxenaire, R., Speich, S., Blanke, B., Chaigneau, A., Pegliasco, C., & Stegner, A. (2018). Anticyclonic eddies connecting the western boundaries of indian and atlantic oceans. *Journal of Geophysical Research: Oceans*.

Laxenaire, R., Speich, S., & Stegner, A. (2019). Evolution of the thermohaline structure of one agulhas ring reconstructed from satellite altimetry and argo floats. *Journal of Geophysical Research*, *124*, 8969-9003.

Laxenaire, R., Speich, S., & Stegner, A. (2020). Agulhas ring heat content and transport in the south atlantic estimated by combining satellite altimetry and argo profiling floats data. *Journal of Geophysical Research*, *125*.

L'Hégaret, P., Carton, X., Louazel, S., & Boutin, G. (2016). Mesoscale eddies and submesoscale structures of persian gulf water off the omani coast in spring 2011. *Ocean Science*, *12*(3), 687–701.

L'Hegaret Pierre, K. J., Speich Sabrina. (2020). *Concatenated temperature, salinity, and velocity measurements from eurec4a_oa/atomic* $ctd, uctd, mvpands - adcpdatafromther/vsl'atalanteandmarias.merian.$ Retrieved from https://www.seanoe.org/data/00809/92071 doi: https://doi.org/10.17882/92071

Liu, T., Abernathey, R. P., Sinha, A., & Chen, D. (2019). Quantifying eulerian eddy leakiness in an idealized model. *Journal of Geophysical Research*, *124*, 8869-8886.

Manta, G., Speich, S., Karstensen, J., Hummels, R., Kersalé, M., Laxenaire, R., ... others (2021). The south atlantic meridional overturning circulation and mesoscale eddies in the first go-ship section at 34.5° s. *Journal of Geophysical Research: Oceans*, *126*(2), e2020JC016962.

Marshall, D. P., Maddison, J. R., & Berloff, P. (2012). A framework for parameterizing eddy potential vorticity fluxes. *Journal of Physical Oceanography*, *42*, 539-557. Retrieved from https://api.semanticscholar.org/CorpusID:55840490

Marshall, D. P., Williams, R. G., & Lee, M.-M. (1999). The relation between eddy-induced transport and isopycnic gradients of potential vorticity. *Journal of Physical Oceanography*, *29*, 1571-1578. Retrieved from https://api.semanticscholar.org/CorpusID:131646498

McWilliams, J. C. (1984). The emergence of isolated coherent vortices in turbulent flow. *Journal of Fluid Mechanics*, *146*, 21–43.

McWilliams, J. C. (1985). Submesoscale, coherent vortices in the ocean. *Reviews of Geophysics*, *23*, 165-182.

McWilliams, J. C. (1989). Statistical properties of decaying geostrophic turbulence. *Journal of Fluid Mechanics*, *198*, 199–230.

Meunier, T., Sanz, E. P., de Marez, C., Pérez, J., Tenreiro, M. F., Angulo, A. R., & Bower, A. (2021). The dynamical structure of a warm core ring as inferred from glider observations and along-track altimetry. *Remote. Sens.*, *13*, 2456.

Nencioli, F., Kuwahara, V. S., Dickey, T. D., Rii, Y. M., & Bidigare, R. R. (2008). Physical dynamics and biological implications of a mesoscale eddy in the lee of hawai'i : Cyclone opal observations during e-flux iii. *Deep-sea Research Part*

Ii-topical Studies in Oceanography, *55*, 1252-1274.

Paillet, J. (1999). Central water vortices of the eastern north atlantic. *Journal of physical oceanography*, *29*(10), 2487–2503.

Paillet, J., Le Cann, B., Carton, X., Morel, Y., & Serpette, A. (2002). Dynamics and evolution of a northern meddy. *Journal of Physical Oceanography*, *32*(1), 55–79.

Pedlosky, J. (1964). The stability of currents in the atmosphere and the ocean: Part i. *Journal of the Atmospheric Sciences*, *21*, 201-219.

Pegliasco, C., Chaigneau, A., & Morrow, R. (2016). Spatio-temporal evolution of two key processes impacting the observed vertical structure of the mesoscale eddies in the 4 major eastern boundary upwelling systems. *American Geophysical Union*, *2016*, PO14D–2836.

Pegliasco, C., Chaigneau, A., Morrow, R., & Dumas, F. (2021). Detection and tracking of mesoscale eddies in the mediterranean sea: A comparison between the sea level anomaly and the absolute dynamic topography fields. *Advances in Space Research*, *68*(2), 401–419.

Penven, P., Halo, I., Pous, S., & Marié, L. (2014). Cyclogeostrophic balance in the mozambique channel. *Journal of Geophysical Research: Oceans*, *119*(2), 1054–1067.

Pierre, L., Xavier, C., Stephanie, L., & Guillaume, B. (2016). Mesoscale eddies and submesoscale structures of persian gulf water off the omani coast in spring 2011. *Ocean Science*, *12(3)*, 687-701. doi: https://doi.org/10.5194/os-12-687-2016

Ripa, P. (1991). General stability conditions for a multi-layer model. *Journal of Fluid Mechanics*, *222*, 119 - 137.

Roshko, A. (1976). Structure of turbulent shear flows: a new look. *AIAA journal*, *14*(10), 1349–1357.

Ruddick, B. R., Oakey, N. S., & Hebert, D. (2010). Measuring lateral heat flux across a thermohaline front: A model and observational test. *Journal of Marine Research*, *68*, 523-539.

Rudnick, D. L. (2001). On the skewness of vorticity in the upper ocean. *Geophysical Research Letters*, *28*.

Shcherbina, A. Y., D'Asaro, E. A., Lee, C. M., Klymak, J. M., Molemaker, M., & McWilliams, J. C. (2013). Statistics of vertical vorticity, divergence, and strain in a developed submesoscale turbulence field. *Geophysical Research Letters*, *40*, 4706–4711.

Stammer, D. (1997). Global characteristics of ocean variability estimated from regional topex/poseidon altimeter measurements. *Journal of Physical Oceanography*, *27*, 1743-1769.

Subirade, C., L'Hégaret, P., Speich, S., Laxenaire, R., Karstensen, J., & Carton, X. (2023). Combining an eddy detection algorithm with in-situ measurements to study north brazil current rings. *Remote Sensing*, *15*(7), 1897.

Tabor, M., & Klapper, I. (1994). Stretching and alignment in chaotic and turbulent flows. *Chaos Solitons & Fractals*, *4*, 1031-1055.

Thomas, L. N., Taylor, J. R., D'Asaro, E. A., Lee, C. M., Klymak, J. M., & Shcherbina, A. (2016). Symmetric instability, inertial oscillations, and turbulence at the gulf stream front. *Journal of Physical Oceanography*, *46*(1), 197–217.

Vortmeyer-Kley, R., Holtermann, P., Feudel, U., & Gräwe, U. (2019). Comparing eulerian and lagrangian eddy census for a tide-less, semi-enclosed basin, the baltic sea. *Ocean Dynamics*, *69*, 701-717.

Wang, Y., Olascoaga, M. J., & Beron-Vera, F. J. (2015). Coherent water transport across the south atlantic. *Geophysical Research Letters*, *42*, 4072 - 4079.

Weiss, J. (1991). The dynamics of entropy transfer in two-dimensional hydrodynamics. *Physica D: Nonlinear Phenomena*, *48*, 273-294.

Wunsch, C. (1999). Where do ocean eddy heat fluxes matter. *Journal of Geophysical Research*, *104*, 13235-13249.

Xia, Q., Li, G., & Dong, C. (2022). Global oceanic mass transport by coherent eddies. *Journal of Physical Oceanography*.

Zaman, K., & Hussain, A. (1981). Taylor hypothesis and large-scale coherent structures. *Journal of Fluid Mechanics*, *112*, 379–396.

Zhang, Z., Tian, J., Qiu, B., Zhao, W., Chang, P., Wu, D., & Wan, X. (2016). Observed 3d structure, generation, and dissipation of oceanic mesoscale eddies in the south china sea. *Scientific Reports*, *6*.

Zhang, Z., Zhong, Y., Tian, J., Yang, Q., & Zhao, W. (2014). Estimation of eddy heat transport in the global ocean from argo data. *Acta Oceanologica Sinica*, *33*, 42-47.

Ōkubo, A. (1970). Horizontal dispersion of floatable particles in the vicinity of velocity singularities such as convergences. *Deep Sea Research and Oceanographic Abstracts*, *17*, 445-454.

Figure 1.

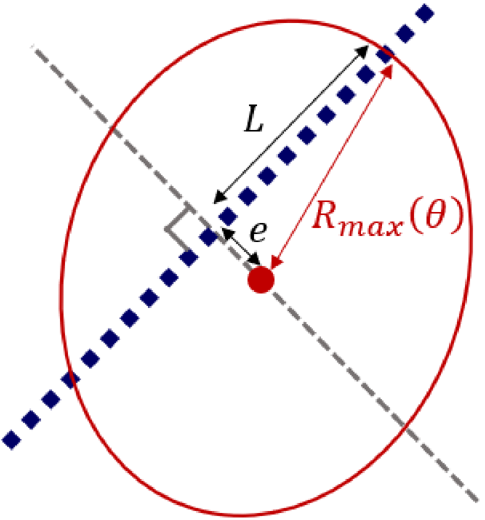

L
e
$R_{max}(\theta)$

Figure 2.

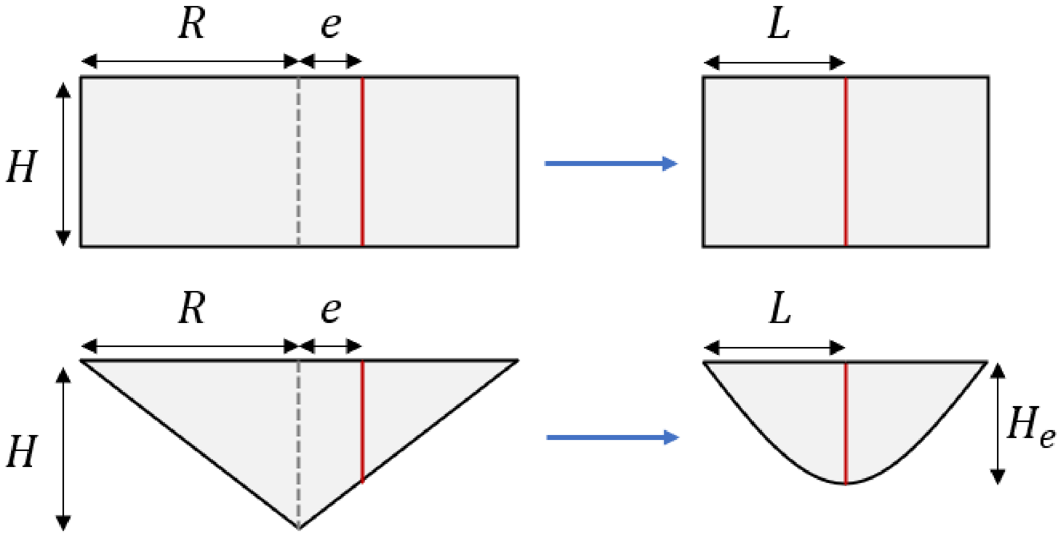

R
e
H
L
R
e
H
L
H_e

Figure 3.

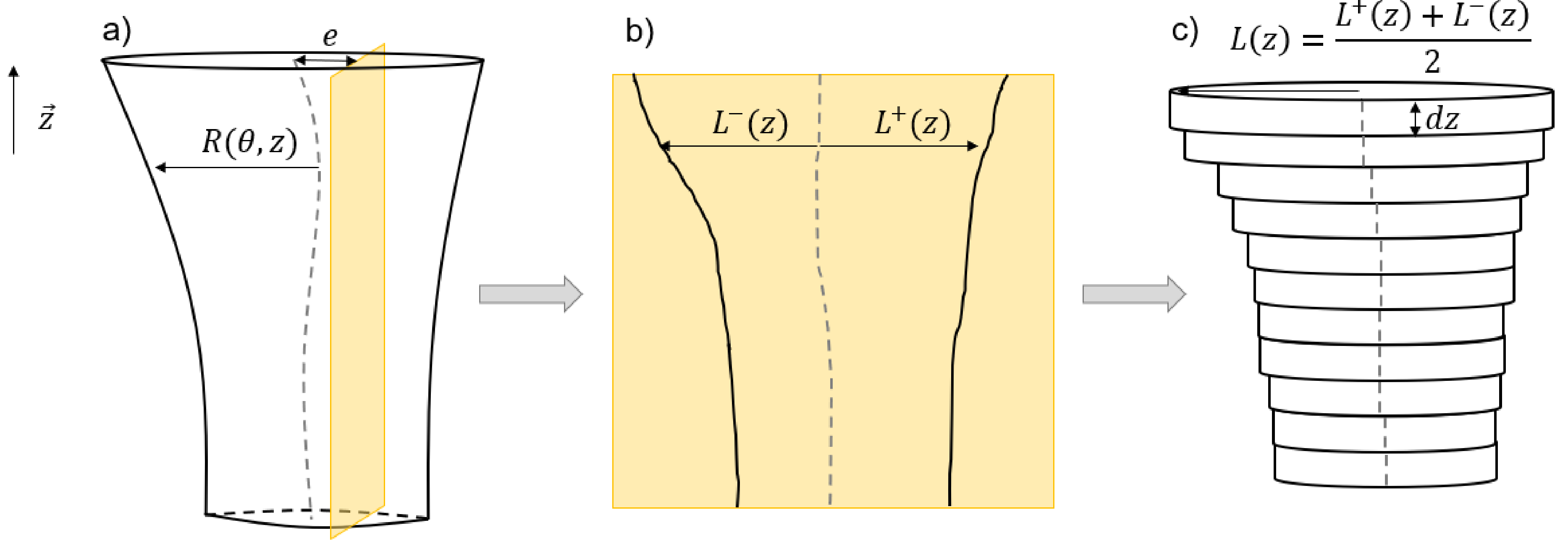
a)
e
$\vec{z}$
$R(\theta, z)$
b)
$L^-(z)$
$L^+(z)$
c)
$L(z) = \frac{L^+(z) + L^-(z)}{2}$
dz

Figure 4.

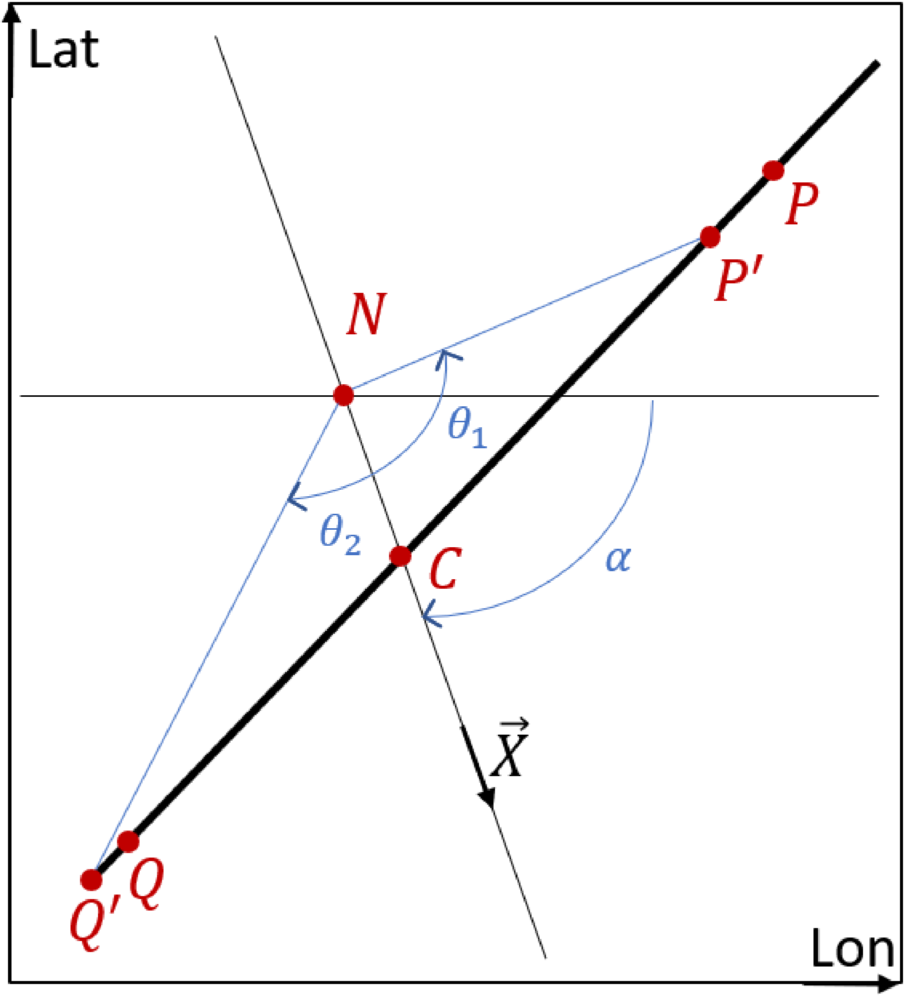
Lat
Lon
P
P'
N
θ_1
θ_2
C
α
$\vec{X}$
Q
Q'

Figure 5.

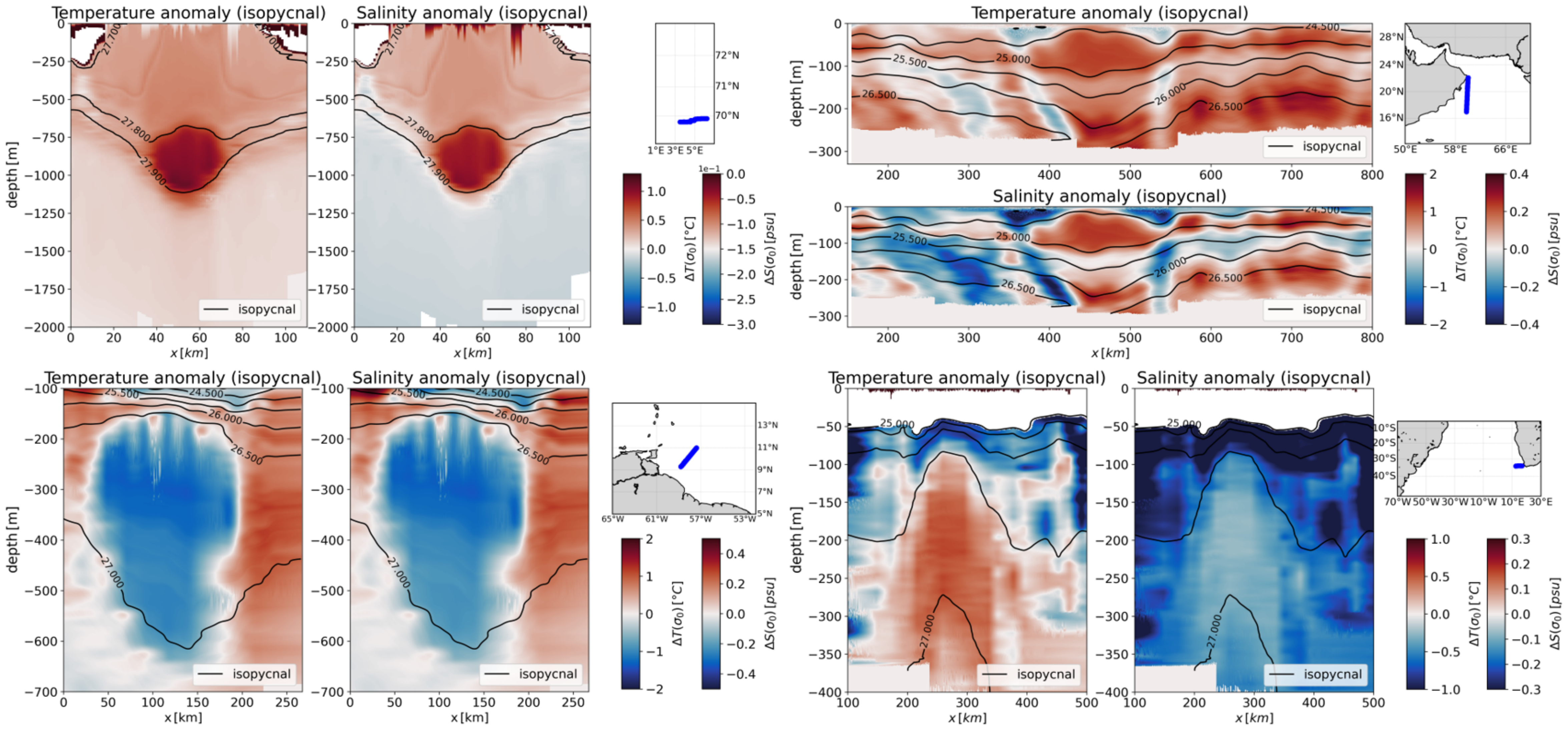
Temperature anomaly (isopycnal)
Salinity anomaly (isopycnal)
depth [m]
x [km]
isopycnal
ΔT(σ0) [°C]
ΔS(σ0) [psu]
72°N
71°N
70°N
1°E 3°E 5°E
28°N
24°N
20°N
16°N
50°E 58°E 66°E
13°N
11°N
9°N
7°N
5°N
65°W 61°W 57°W 53°W
10°S
20°S
30°S
40°S
70°W 50°W 30°W 10°W 10°E 30°E

Figure 6.

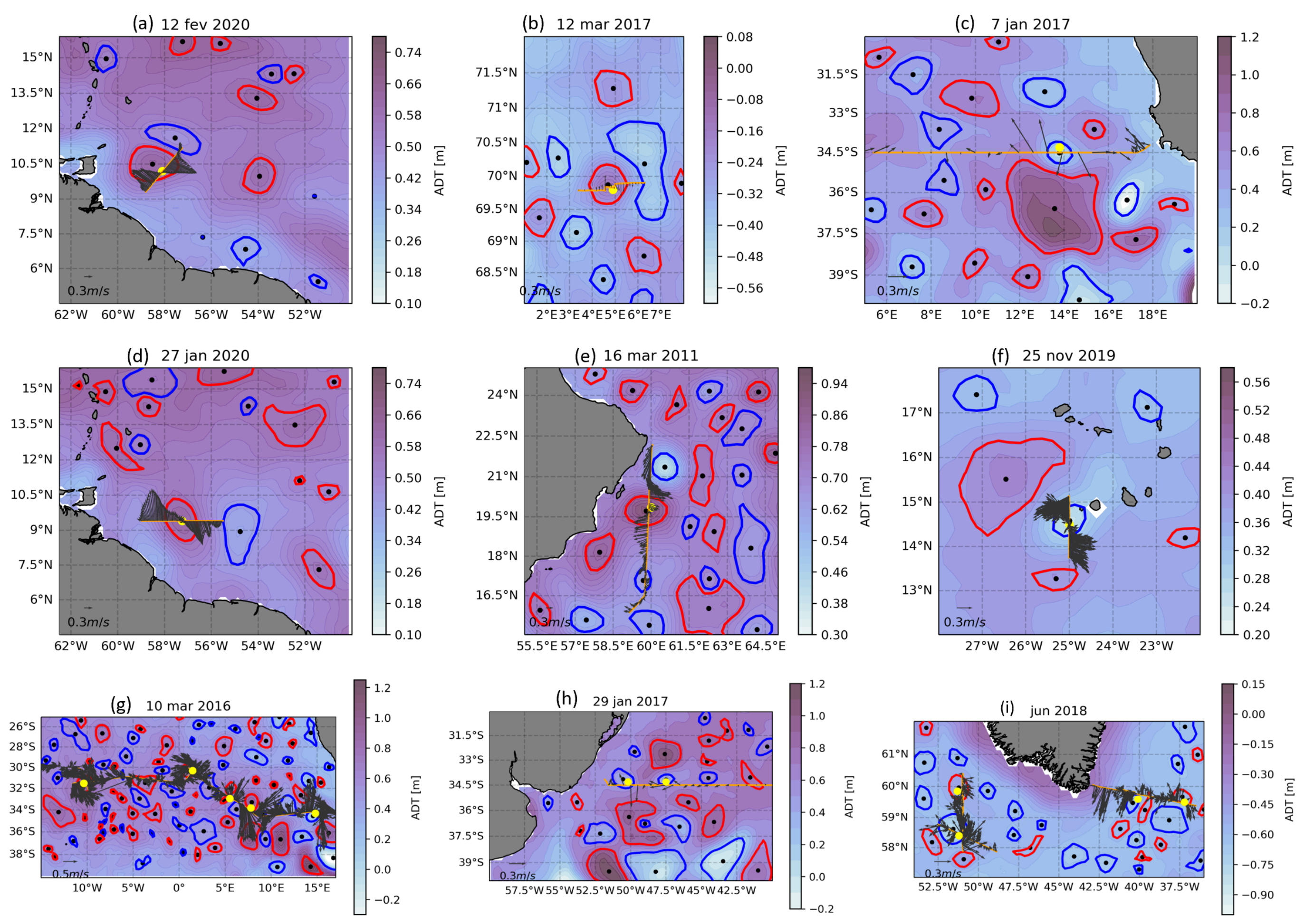

(a) 12 fev 2020
(b) 12 mar 2017
(c) 7 jan 2017
(d) 27 jan 2020
(e) 16 mar 2011
(f) 25 nov 2019
(g) 10 mar 2016
(h) 29 jan 2017
(i) jun 2018
ADT [m]
0.3m/s
0.5m/s

Figure 7.

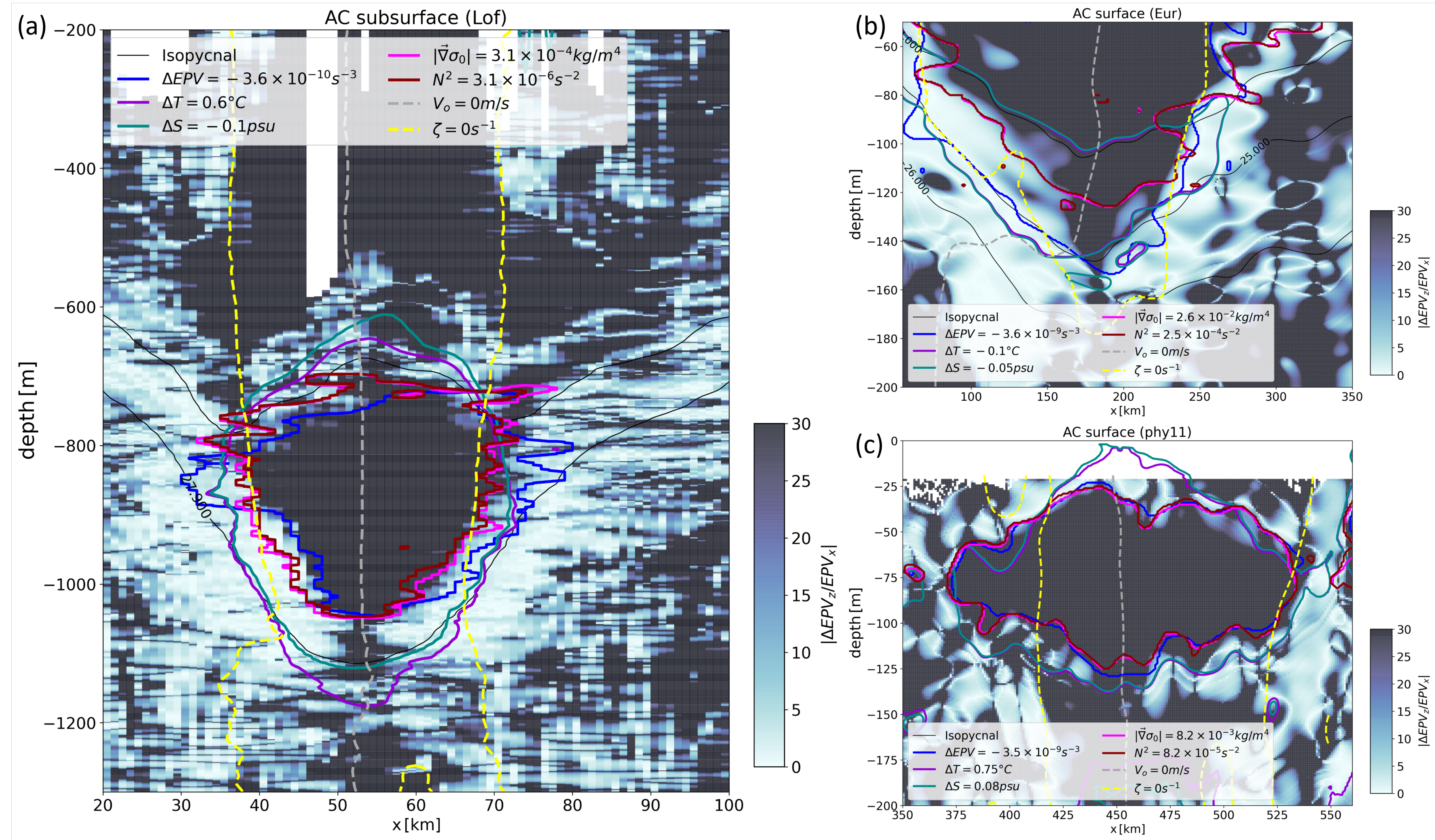

(a)
AC subsurface (Lof)
Isopycnal
ΔEPV = −3.6 × 10⁻¹⁰ s⁻³
ΔT = 0.6°C
ΔS = −0.1psu
|∇σ₀| = 3.1 × 10⁻⁴ kg/m⁴
N² = 3.1 × 10⁻⁶ s⁻²
V_o = 0m/s
ζ = 0s⁻¹
depth [m]
x [km]
|ΔEPV_z/EPV_x|
(b)
AC surface (Eur)
25.000
26.000
Isopycnal
ΔEPV = −3.6 × 10⁻⁹ s⁻³
ΔT = −0.1°C
ΔS = −0.05psu
|∇σ₀| = 2.6 × 10⁻² kg/m⁴
N² = 2.5 × 10⁻⁴ s⁻²
V_o = 0m/s
ζ = 0s⁻¹
depth [m]
x [km]
|ΔEPV_z/EPV_x|
(c)
AC surface (phy11)
Isopycnal
ΔEPV = −3.5 × 10⁻⁹ s⁻³
ΔT = 0.75°C
ΔS = 0.08psu
|∇σ₀| = 8.2 × 10⁻³ kg/m⁴
N² = 8.2 × 10⁻⁵ s⁻²
V_o = 0m/s
ζ = 0s⁻¹
depth [m]
x [km]
|ΔEPV_z/EPV_x|

Figure 8.

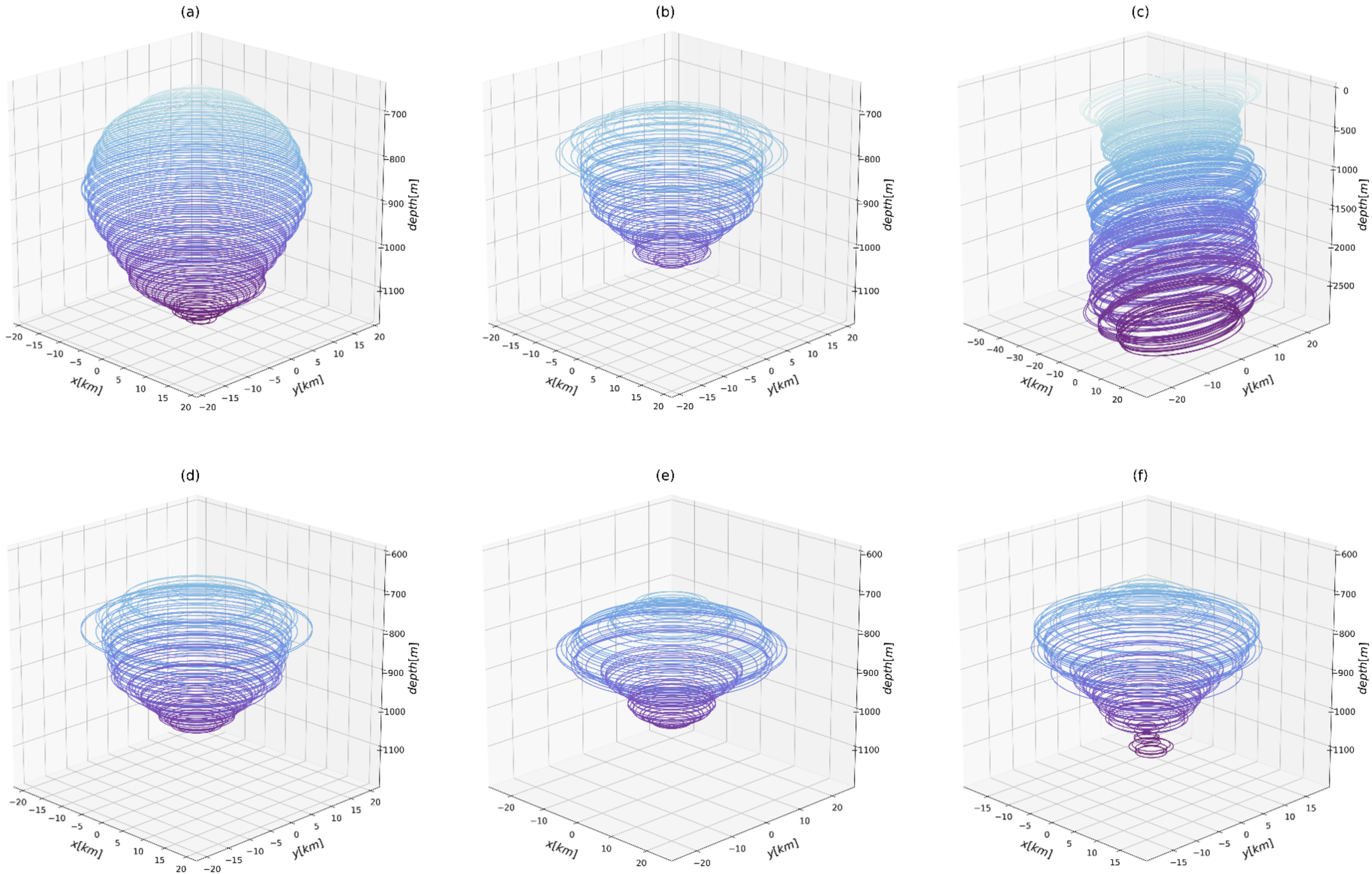
(a)
700
800
900
1000
1100
depth[m]
x[km]
y[km]
(b)
700
800
900
1000
1100
depth[m]
x[km]
y[km]
(c)
0
500
1000
1500
2000
2500
depth[m]
x[km]
y[km]
(d)
600
700
800
900
1000
1100
depth[m]
x[km]
y[km]
(e)
600
700
800
900
1000
1100
depth[m]
x[km]
y[km]
(f)
600
700
800
900
1000
1100
depth[m]
x[km]
y[km]

Figure 9.

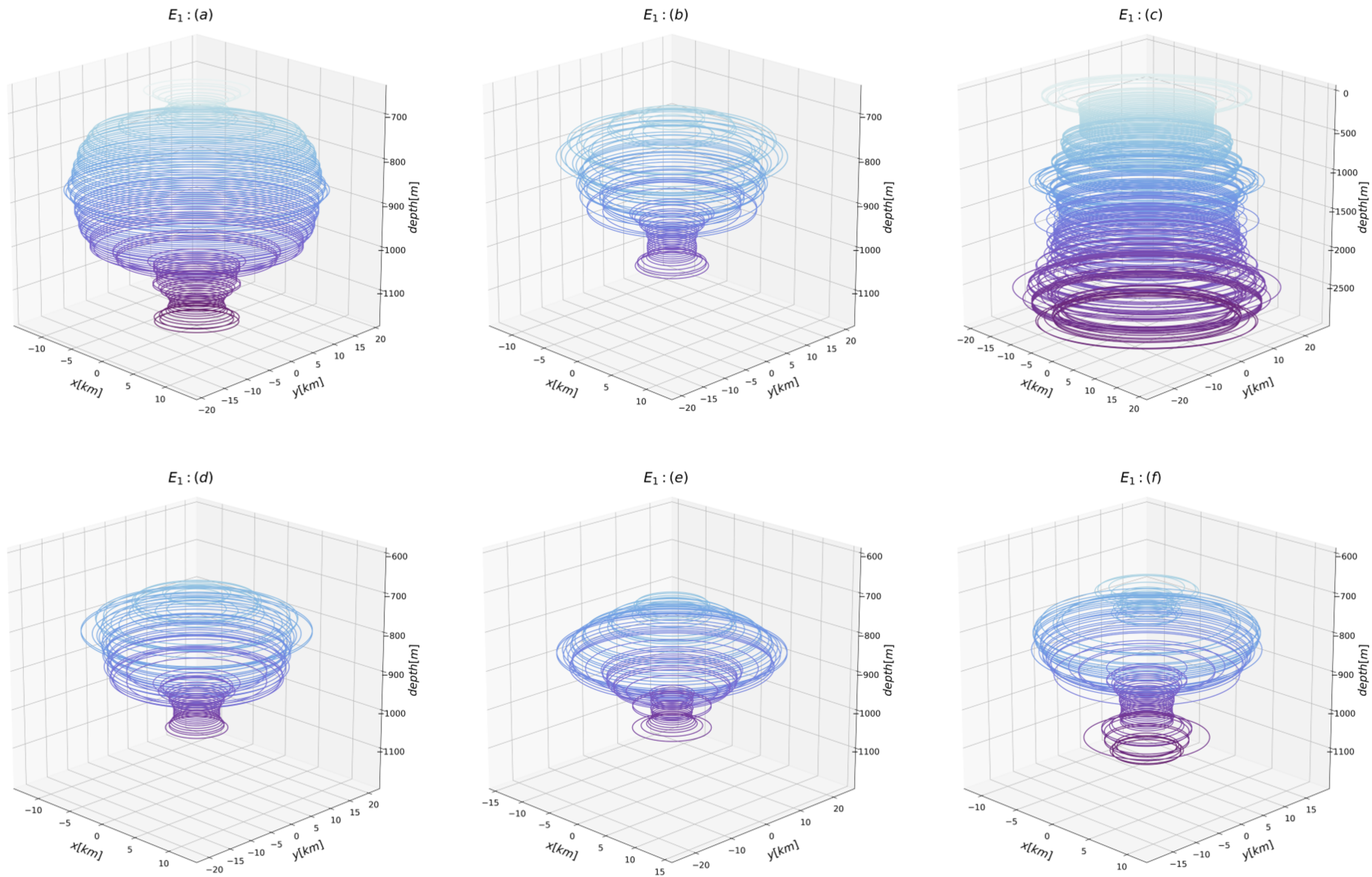

$E_1:(a)$
$E_1:(b)$
$E_1:(c)$
$E_1:(d)$
$E_1:(e)$
$E_1:(f)$
x[km]
y[km]
depth[m]

Figure 10.

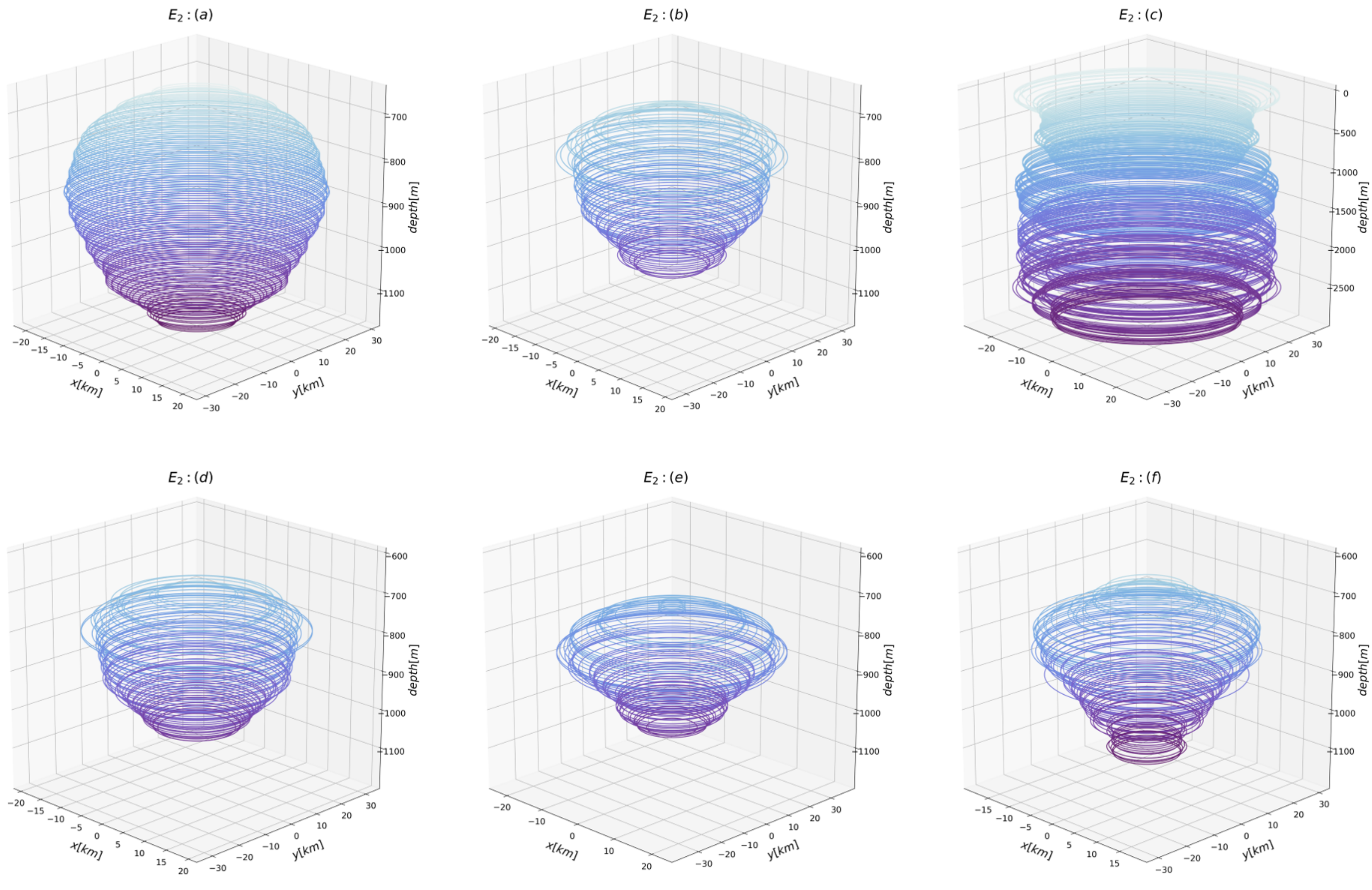

$E_2:(a)$
$E_2:(b)$
$E_2:(c)$
$E_2:(d)$
$E_2:(e)$
$E_2:(f)$
x[km]
y[km]
depth[m]

Figure 11.

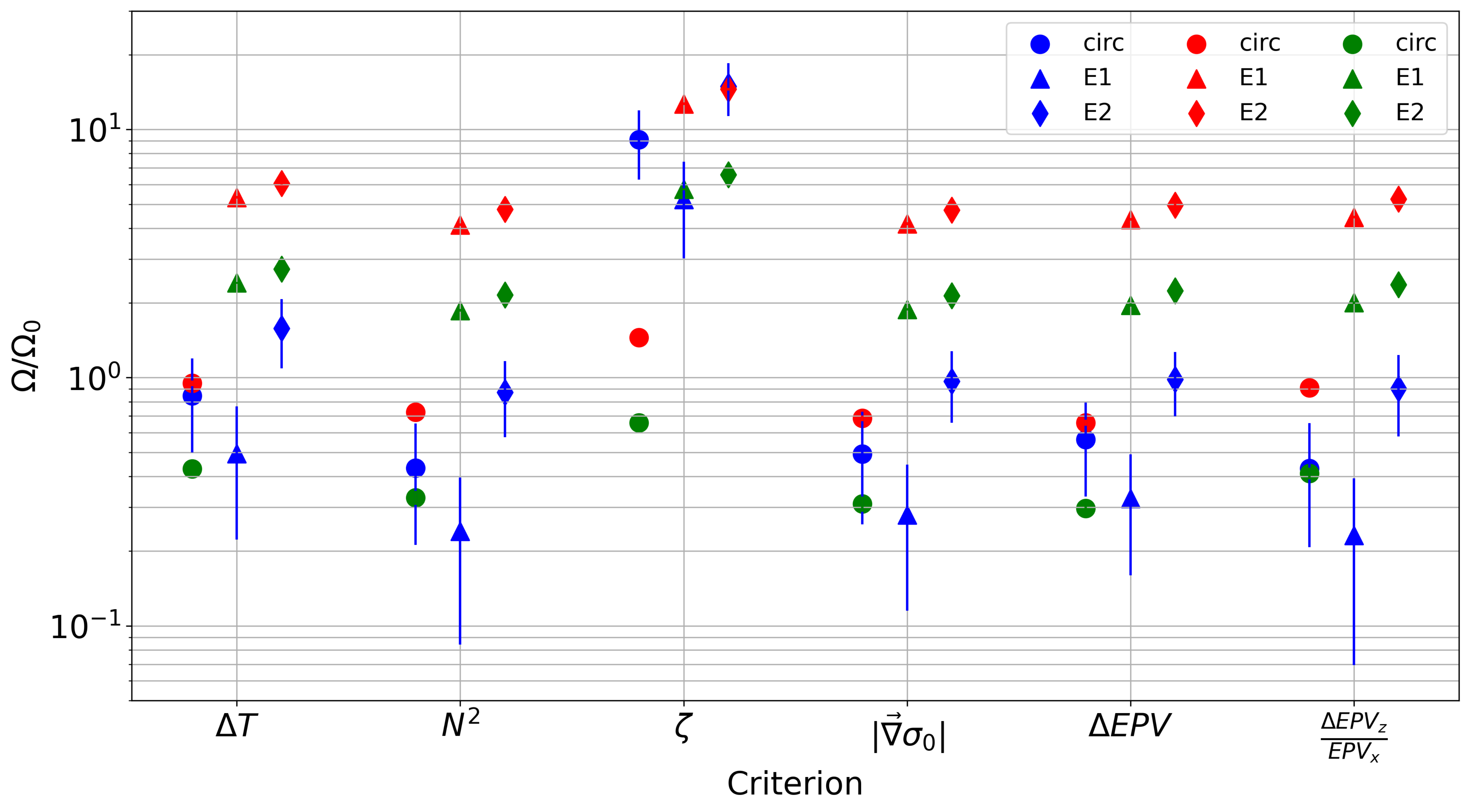

circc
E1
E2
circ
E1
E2
circ
E1
E2
10^1
10^0
10^{-1}
Ω/Ω_0
ΔT
N^2
ζ
$|\vec{\nabla}\sigma_0|$
ΔEPV
$\frac{\Delta EPV_z}{EPV_x}$
Criterion

Figure 12.

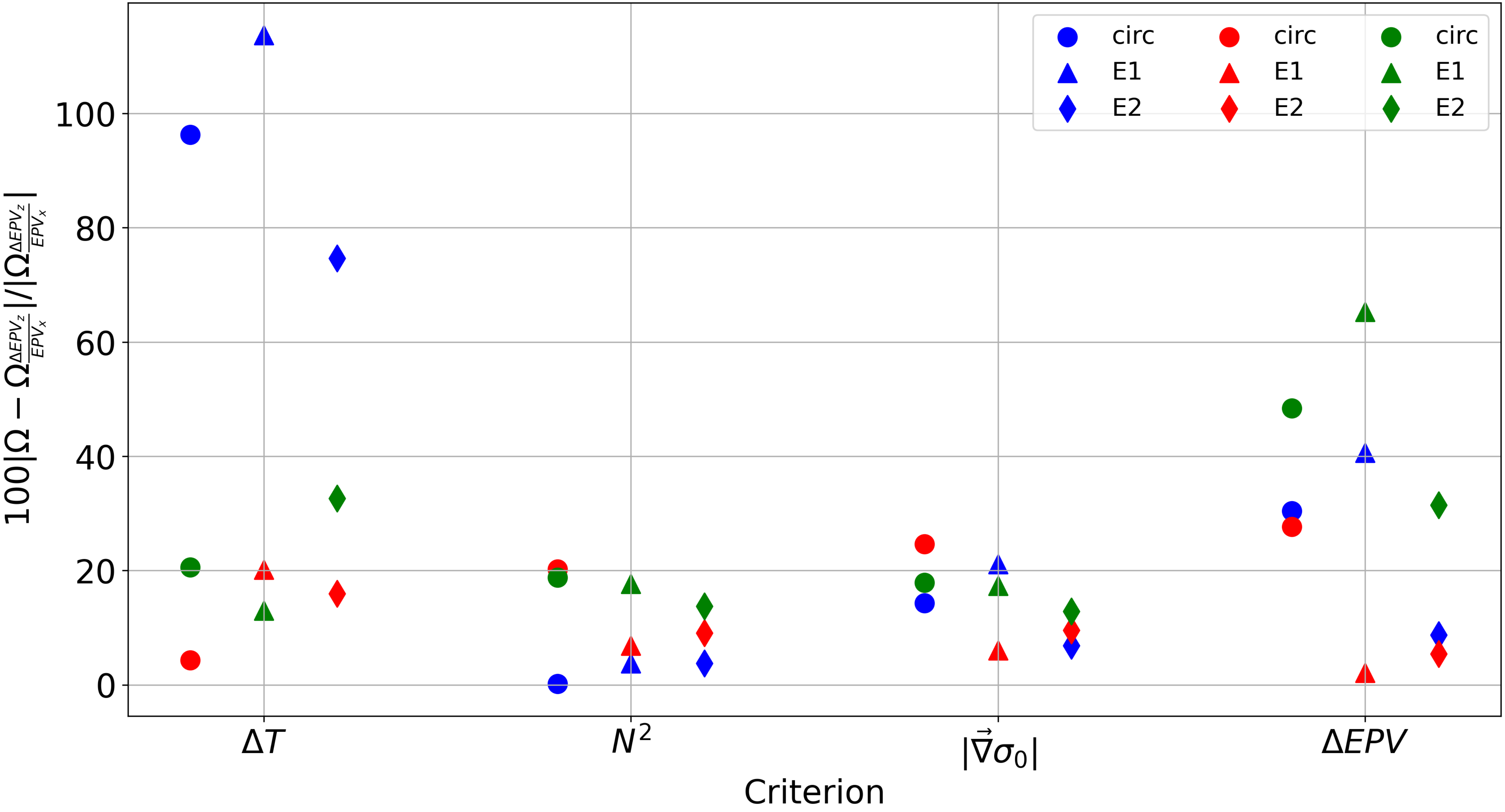

circ
E1
E2
circ
E1
E2
circ
E1
E2
100
80
60
40
20
0
$100|\Omega - \Omega_{\frac{\Delta EPV_z}{EPV_x}}|/|\Omega_{\frac{\Delta EPV_z}{EPV_x}}|$
ΔT
N^2
$|\vec{\nabla}\sigma_0|$
ΔEPV
Criterion